Cell Reports

Article

Met/HGFR triggers detrimental reactive microglia in TBI

Graphical abstract

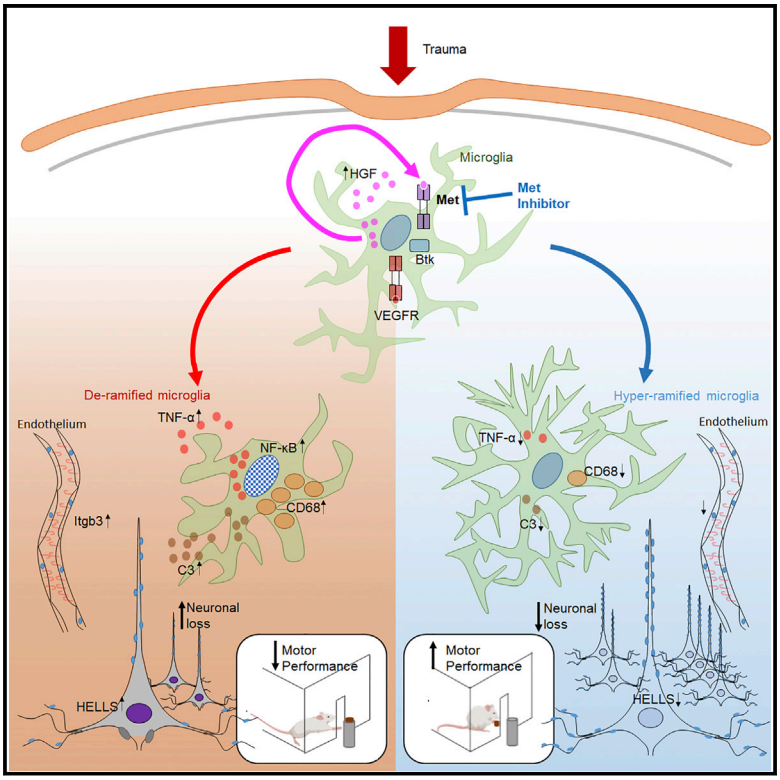

Highlights

- TBI is associated with complex, time-dependent patterns of RTK activation
- Met is activated in microglia upon TBI, and Met inhibition decreases microglia reaction
- Blockade of Met reduces acute and sub-acute motor impairment due to TBI
- The Met inhibitor reduces synaptic and neuronal loss after TBI

Authors

Rida Rehman, Michael Miller, Sruthi Sankari Krishnamurthy, ..., Maria Cristina Morganti-Kossmann, Aya Takeoka, Francesco Roselli

Correspondence

francesco.roselli@uni-ulm.de

In brief

Controlling neuroinflammation in neurotrauma is an important but unachieved goal. Rehman et al. exploit a moderate TBI model and array-based proteomics to identify Met/HGFR as an inducer of reactive microglia. A small-molecule inhibitor of Met/HGFR suppresses microglial reactivity, reduces neuronal and vascular alterations, limits behavioral disturbances, and accelerates recovery.

Rehman et al., 2022, Cell Reports *41*, 111867
December 27, 2022
https://doi.org/10.1016/j.celrep.2022.111867

CellPress

Cell Reports

CellPress
OPEN ACCESS

Article

Met/HGFR triggers detrimental reactive microglia in TBI

Rida Rehman,[1] Michael Miller,[2,3] Sruthi Sankari Krishnamurthy,[1] Jacob Kjell,[4,5] Lobna Elsayed,[1] Stefanie M. Hauck,[6] Florian olde Heuvel,[1] Alison Conquest,[7] Akila Chandrasekar,[1,8] Albert Ludolph,[1,9] Tobias Boeckers,[9,10] Medhanie A. Mulaw,[11] Magdalena Goetz,[4] Maria Cristina Morganti-Kossmann,[7,12] Aya Takeoka,[2,3,13] and Francesco Roselli[1,9,14,*]

[1]Department of Neurology, Ulm University, Ulm, Germany
[2]VIB-Neuroelectronics Research Flanders (NERF), Leuven, Belgium
[3]KU Leuven, Department of Neuroscience and Leuven Brain Institute, Leuven, Belgium
[4]Institute for Stem Cell Research, Helmholtz Zentrum München & Biomedical Center, Ludwig-Maximilians Universitaet, Planegg-Martinsried, Germany
[5]Department of Clinical Neuroscience, Karolinska Institutet, Solna, Sweden
[6]Research Unit Protein Science and Metabolomics and Proteomics Core Facility, Helmholtz Zentrum Munich, Munich, Germany
[7]National Trauma Research Institute and Department of Neurosurgery, The Alfred Hospital, Melbourne, VIC, Australia
[8]Institute of Experimental Pharmacology and Toxicology, University of Lübeck, Lübeck, Germany
[9]German Center for Neurodegenerative Diseases (DZNE), Ulm, Germany
[10]Institute of Anatomy and Cell Biology, Ulm University, Ulm Germany
[11]Unit for Single-cell Genomics, Medical Faculty, Ulm University, Ulm, Germany
[12]Department of Epidemiology and Preventive Medicine, Monash University, Melbourne, VIC, Australia
[13]Interuniversity Microelectronics Centre-IMEC, Leuven, Belgium
[14]Lead contact
*Correspondence: francesco.roselli@uni-ulm.de
https://doi.org/10.1016/j.celrep.2022.111867

SUMMARY

The complexity of signaling events and cellular responses unfolding in neuronal, glial, and immune cells upon traumatic brain injury (TBI) constitutes an obstacle in elucidating pathophysiological links and targets for intervention. We use array phosphoproteomics in a murine mild blunt TBI to reconstruct the temporal dynamics of tyrosine-kinase signaling in TBI and then scrutinize the large-scale effects of perturbation of Met/HGFR, VEGFR1, and Btk signaling by small molecules. We show Met/HGFR as a selective modifier of early microglial response and that Met/HGFR blockade prevents the induction of microglial inflammatory mediators, of reactive microglia morphology, and TBI-associated responses in neurons and vasculature. Both acute and prolonged Met/HGFR inhibition ameliorate neuronal survival and motor recovery. Early elevation of HGF itself in the cerebrospinal fluid of TBI patients suggests that this mechanism has translational value in human subjects. Our findings identify Met/HGFR as a modulator of early neuroinflammation in TBI with promising translational potential.

INTRODUCTION

Traumatic brain injury (TBI) is characterized by complex and dynamic responses unfolding in neurons, glia, endothelial cells, and infiltrating leukocytes[1] from hours (acute phase) to weeks (chronic phase). Among the very first events following TBI, microglia increase motility, retract processes, and migrate toward the site of damage.[2–6] Detrimental consequences of acute microglial responses include local acidosis,[7] oxidative stress,[8] and synaptic silencing,[9] all contributing to the "secondary damage"[10] occurring hours to days after the mechanical lesion. Beneficial effects of microglia have also been studied[3] including the sealing of the disrupted glia limitans,[5] clearing of debris,[11] and the stimulation of neurogenesis.[12] Damage-associated molecular patterns driving reactive microglia upon brain damage include ATP,[5,13] interferons, complement factors,[14,15] and inflammatory cytokines.[13] This remains true also in the case of comparatively mild TBI, which can nevertheless lead to long-term consequences.[10,16] Therefore, it remains important to comprehensively characterize the mediators driving microglial reactivity in mild TBI to identify new entry points and fine tune microglial responses toward beneficial outcomes.

A substantial number of receptor and non-receptor tyrosine kinases (RTK and NRTK, respectively) are abundantly expressed in microglia and endothelial cells.[17,18] Functional relevance in microglial reactivity has been established only for a few RTKs: Axl decreases microglial reactivity in inflammatory conditions and drives debris phagocytosis,[4,19] whereas MCSFR1 (c-Fms, CSFR1) reportedly determines microglial survival and proliferation.[20,21] Nevertheless, microglia express a substantial number

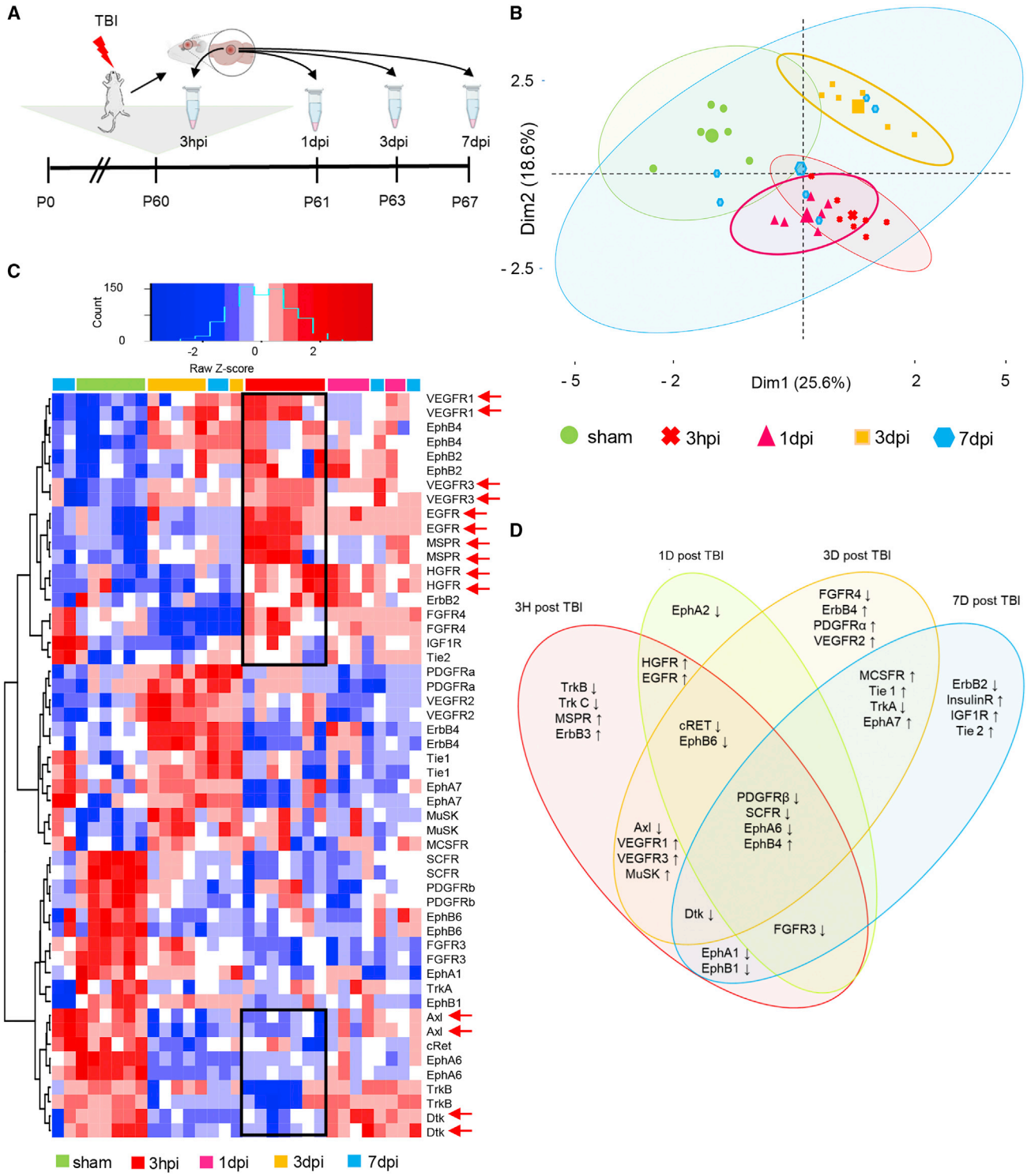

Figure 1. Dynamic RTK phosphorylation pattern post trauma

(A) Outline of the experimental design. Mice were subjected to trauma and samples were collected at 3 hpi, 1 dpi, 3 dpi, and 7 dpi (hpi: hours post injury, dpi: days post injury).

(B) Post-preprocessing PCA plot depicts distinct clustering of each group with 95% confidence ellipses around the groups. All groups showed minimal overlap except 7 dpi, displaying substantial variability. Small symbols represent individual animals. Large symbols indicate the weighted average for each subgroup.

(C) Heatmap displays unsupervised clustering of differentially phosphorylated RTKs at different timepoints. The arrows highlight prominent receptors.

(legend continued on next page)

of RTKs (including neurotrophins and growth factors receptors)[17,18,22] potentially involved in early reactivity upon tissue damage.

Importantly, RTK/NRTK are potential entry points for therapeutic modulation of TBI-induced neuroinflammation, with more than 30 RTK/NRTK inhibitors already in clinical use[23] lending themselves to drug repurposing efforts. Here, we have employed large-scale phosphoproteomic arrays to understand the temporal activation of RTKs and NRTKs in trauma and identify new regulators of TBI-induced neuroinflammation. We have identified the RTK cMet/HGFR (here on as Met) as a new player involved in acute microglial activation in TBI. We demonstrate that a small-molecule inhibitor (Inh) of Met is able to prevent inflammatory signaling, limit microglial recruitment, reduce neuronal and vascular distress, and acutely improve neurological function upon TBI.

RESULTS

Large-scale dynamics of RTK phosphorylation in the cerebral cortex upon TBI

We explored the injury-related architecture of RTK signaling in a murine model of mild TBI. In our weight-drop mild (NSS 0–1)[14] blunt head trauma model, neuronal counts were normal 3 h post injury (hpi), but significantly declined in the injury core at 3 days post injury (dpi) (21.1% ± 15.4% of NeuN+ cells lost in the core [c] lesion, layer II-III; Figure S1A, $p = 0.0103$ vs. sham; Figures S1B and S1C), and this decline increases further at 7 dpi (95.5% ± 3.3% in the core [c]; $p < 0.0001$ vs. sham).

First, we monitored, using nitrocellulose antibody arrays, the phosphorylation of 39 RTKs in cortical samples obtained at 3 hpi (n = 7), 1 dpi (n = 6), 3 dpi (n = 6), or 7 dpi (n = 6) compared with sham controls (n = 6) (Figure 1A). Principal component analysis (PCA) revealed a clear separation of the sham, 3 hpi, 1 dpi, and 3 dpi samples, whereas 7 dpi samples displayed substantial variability (Figure 1B). A distinct pattern of RTK phosphorylation for each time point considered was detected using modified analysis algorithms (Figures 1C and 1D, see also Data S1, See STAR Methods section array analyses for details).

The RTK phosphorylation profiles at 3 hpi and 1 dpi displayed the largest divergence from the sham but were otherwise similar to each other. VEGFR1, VEGFR3, EphB4, Met, MSPR, EGFR, ErbB3, and MuSK were up-phosphorylated, whereas TrkB, TrkC, Axl, Dtk, SCFR/c-kit, PDGFRb, cRET, EphA1, EphA6, EphB1, and EphB6 were down-phosphorylated (phosphorylated here on as "p"). At 3 dpi, the RTK profile was characterized by increase in phosphorylation of ErbB4, PDGFRa, and VEGFR2 and down-phosphorylation of FGFR4, Axl, and cRet. Despite the substantial variability observed at 7 dpi, possibly indicating an inter-individual divergence in the sub-acute phase, we detected a statistically significant increase in phosphorylation levels of insulin receptor1, Tie2, and IGFR1 and down-phosphorylation in ErbB2 (Figure 1D).

Notably, at least five of the RTKs modulated at 3 hpi regulate microglial reactivity. Axl, Dtk, and c-kit/SCFR were down-phosphorylated (corresponding to microglial reactivity[4,24]; Figure S1D), whereas Met/HGFR and MSPR (involved in chemotaxis[25,26]) were strongly up-phosphorylated (Figure S1E).

Other RTK families followed unique dynamics upon TBI. VEGFR1 and VEGFR3 were up-phosphorylated at 3 hpi and 3 dpi, whereas VEGFR2 was only up-phosphorylated at 3 dpi (Figure S1F). A significant and time-dependent increase in phosphorylation was observed also for receptors in the EGFR/ErbB family, insulin/IGFIR family, and most notably in the ephrin family members (Figures 1D and S1G).

Notably, the RTK phosphorylation pattern was influenced by the severity of the injury. From an independent set of animals, brain samples from a milder trauma (total energy = 0.47 J), when compared with those from standard trauma (total energy = 0.53 J) or sham controls, displayed a phosphorylation pattern intermediate between sham and standard-trauma samples (Figure S1H). Interestingly, the milder trauma samples displayed an increased, rather than decreased, phosphorylation of Dtk and Axl, whereas phosphorylation levels of Met and VEGFR3 were still significantly upregulated (Figure S1H).

In-depth characterization of tyrosine-kinase signaling network upon acute TBI

In order to confirm and extend the data from the chemiluminescence arrays, and to identify signaling cascades downstream of activated RTK, we profiled the tyrosine phosphorylation of 228 distinct targets in somatosensory cortex of sham-operated (Sham, n = 3) or TBI (Sal TBI, n = 3) mice at 3 hpi (NSS 0–1) using a fluorescence antibody array (Figure 2A). PCA demonstrated a remarkable separation of sham and TBI ellipses (95% confidence interval; Figure 2B). After a cutoff value of $2*\log10^2$ was applied, 39 proteins showed significant differences in tyrosine phosphorylation upon trauma (Figure 2C, see also Data S2) including VEGFR1, EGFR, and Met already shown by the chemiluminescence screening (cf. Figures 1C and 1D and 2C). Notably, several NRTK and other signaling molecules with altered phosphorylation upon TBI (such as Btk, Hck, DAPP1, Blnk, Vav1, and Plcg2) are involved in microglial function,[27–30] whereas a smaller set of hits was attributed to neuronal signaling (NMDAR1 NR2A/2B, Kv1.3, and alpha-synuclein; Figure 2C).

We confirmed the cellular specificity of the phosphorylation of pMet (Tyr1234), pBTK (Tyr222), and pVEGFR1 (Tyr1333) by immunostaining. Immunoreactivity for pMet and pBTK was almost undetectable in sham brains but was significantly increased upon TBI. Notably, in TBI nearly all immunoreactivity was restricted to Iba1+ cells (Figures 2D and 2E, pMet; $p < 0.0001$ vs. Sham and pBtk; $p = 0.0001$ vs. Sal sham). Neurons displayed very weak immunostaining for pMet and pBtk with no increase in phosphorylation after trauma (Figures S2A and S2B and 2F). On the contrary, immunoreactivity for pVEGFR1 was upregulated in vessels, microglia, and neurons upon TBI (Figures 2D–2F, pVEGFR1; microglia: $p = 0.0044$ vs. Sal sham, neurons: $p = 0.0128$ vs. Sal sham, Figures S2C and S2D).

(D) Venn diagram summarizes overlap of significant RTKs at different timepoints compared with sham. In (B)–(D), n = 6 for sham, 1 dpi, 3 dpi, and 7 dpi, and n = 7 for 3 hpi (hpi: hours post injury, dpi: days post injury). Significance for differentially expressed (DE) proteins was set at $p < 0.05$ (false discovery rate [FDR] adjusted). Detailed comparisons are shown in Data S1. Also see Figure S1.

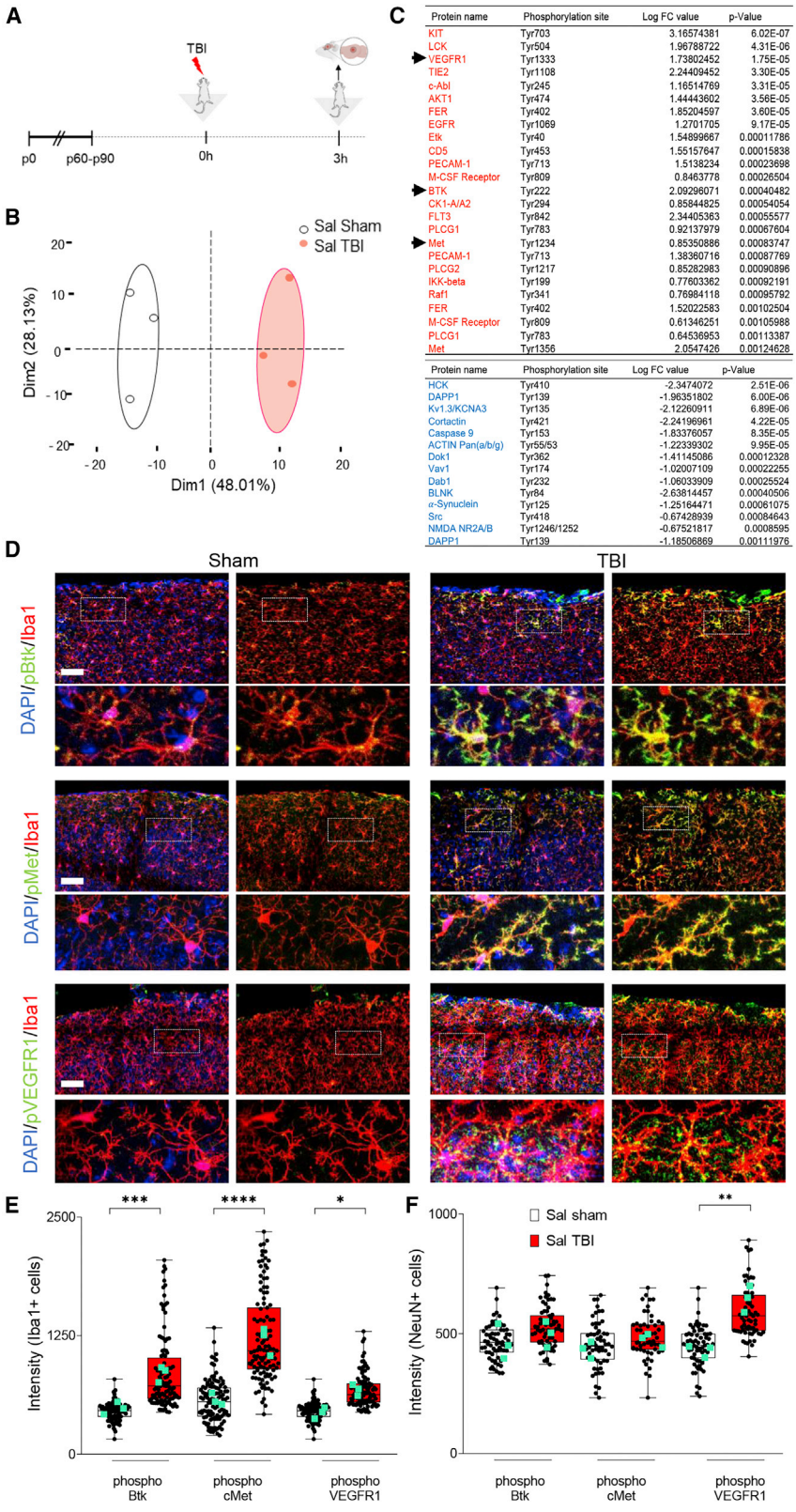

Protein name	Phosphorylation site	Log FC value	p-Value
KIT	Tyr703	3.16574381	6.02E-07
LCK	Tyr504	1.96788722	4.31E-06
VEGFR1	Tyr1333	1.73802452	1.75E-05
TIE2	Tyr1108	2.24409452	3.30E-05
c-Abl	Tyr245	1.16514769	3.31E-05
AKT1	Tyr474	1.44443602	3.56E-05
FER	Tyr402	1.85204597	3.60E-05
EGFR	Tyr1069	1.2701705	9.17E-05
Etk	Tyr40	1.54899667	0.00011786
CD5	Tyr453	1.55157647	0.00015838
PECAM-1	Tyr713	1.5138234	0.00023698
M-CSF Receptor	Tyr809	0.8463778	0.00026504
BTK	Tyr222	2.09296071	0.00040482
CK1-A/A2	Tyr294	0.85844825	0.00054054
FLT3	Tyr842	2.34405363	0.00055577
PLCG1	Tyr783	0.92137979	0.00067604
Met	Tyr1234	0.85350886	0.00083747
PECAM-1	Tyr713	1.38360716	0.00087769
PLCG2	Tyr1217	0.85282983	0.00090896
IKK-beta	Tyr199	0.77603362	0.00092191
Raf1	Tyr341	0.76984118	0.00095792
FER	Tyr402	1.52022583	0.00102504
M-CSF Receptor	Tyr809	0.61346251	0.00105988
PLCG1	Tyr783	0.64536953	0.00113387
Met	Tyr1356	2.0547426	0.00124628

Protein name	Phosphorylation site	Log FC value	p-Value
HCK	Tyr410	-2.3474072	2.51E-06
DAPP1	Tyr139	-1.96351802	6.00E-06
Kv1.3/KCNA3	Tyr135	-2.12260911	6.89E-06
Cortactin	Tyr421	-2.24196961	4.22E-05
Caspase 9	Tyr153	-1.83376057	8.35E-05
ACTIN Pan(a/b/g)	Tyr55/53	-1.22339302	9.95E-05
Dok1	Tyr362	-1.41145086	0.00012328
Vav1	Tyr174	-1.02007109	0.00022255
Dab1	Tyr232	-1.06033909	0.00025524
BLNK	Tyr84	-2.63814457	0.00040506
α-Synuclein	Tyr125	-1.25164471	0.00061075
Src	Tyr418	-0.67428939	0.00084643
NMDA NR2A/B	Tyr1246/1252	-0.67521817	0.0008595
DAPP1	Tyr139	-1.18506869	0.00111976

Figure 2. In-depth tyrosine kinase screening 3 hpi and identifying microglia as key player

(A) Outline of the experiment.

(B) Post-preprocessing PCA plot shows distinct clustering of groups with no overlap between the confidence ellipses with PC1 contributing to 48%.

(C) List of DE proteins ($p \leq 0.05$) up-phosphorylated (red) or down-phosphorylated (blue) at 3 hpi compared with baseline (TBI vs. sham) with logarithmic fold change and individual significance.

(D–F) pBtk, pMet, and pVEGFR1 colocalized with microglia (Iba1+ cells) and upregulation in Sal TBI compared with Sal sham (see also Figure S2 for neuronal and vascular overlap of the phosphorylated proteins). Phosphorylated receptors were expressed in (E) Iba1+ cells (microglia) or (F) NeuN+ cells (neurons) verifying the screening results. In (A)–(C), n = 3/group. Significance for DE proteins was set at $p < 0.05$ (Benjamini-Hochberg adjusted). Detailed individual comparisons are shown in Data S2. In (D)–(F), n = 4/group. Dots indicate individual values for each cell. Significance of differences between means were analyzed using two-way ANOVA with Sidak correction. (*$p < 0.05$, **$p < 0.001$, ***$p < 0.001$, ****$p < 0.0001$). Scale bars: 300 μm for (D). Boxplots display the 25–75 percentile interval (box contours) and the full range (whiskers).

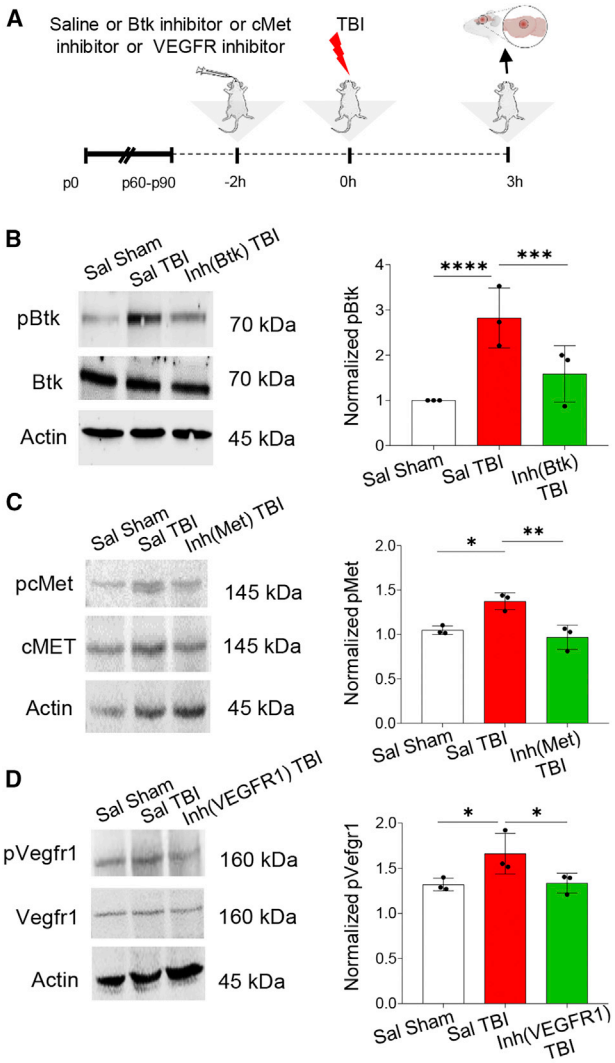

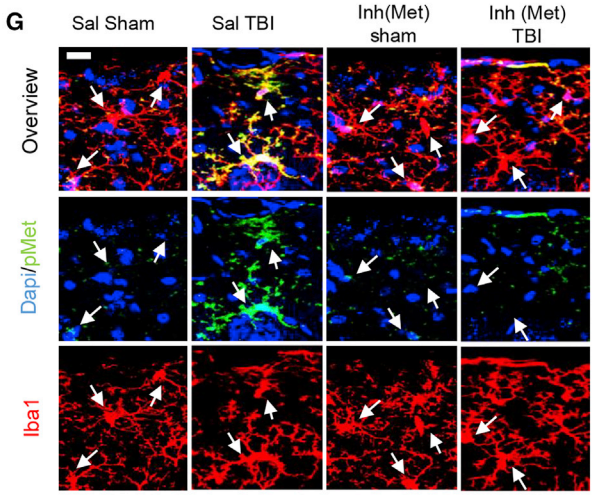

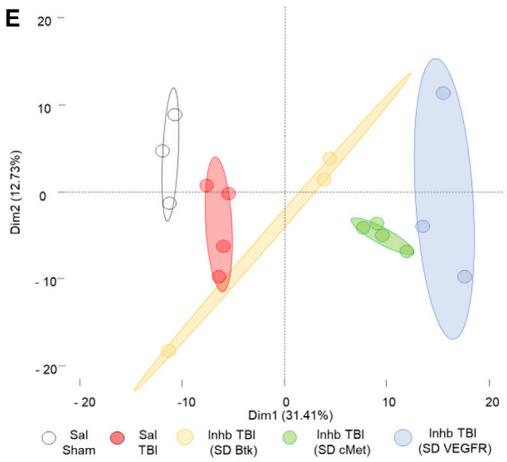

F

Protein Name	Phosphorylation site	Log FC	p-Value
HRS	Tyr334	-3.16574381	6.02E-07
HRS	Tyr334	-1.96788722	4.31E-06
EGFR	Tyr1069	-1.73802452	1.75E-05
PDGFRa	Tyr849	-2.24409452	3.30E-05
IR	Tyr1361	-1.16514769	3.31E-05
BTK	Tyr550	-1.44443602	3.56E-05
PLGC2	Tyr753	-1.85204597	3.60E-05
EGFR	Tyr1069	-1.2701705	9.17E-05
Kit	Tyr703	-1.54899667	0.00011786
cJun	Tyr170	-1.55157647	0.00015838
IL3R	Tyr593	1.5138234	0.00023698
BLNK	Tyr96	0.8463778	0.00026504
BLNK	Tyr96	2.09296071	0.00040482
TFII	Tyr248	0.85844825	0.00054054
Pyk2	Tyr580	2.34405363	0.00055577
Caveolin	Tyr14	0.92137979	0.00067604
PI3K subunit a/g	Tyr467.199	0.85350886	0.00083747
VEGFR2	Tyr1175	1.38360716	0.00087769
Gab2	Tyr643	0.77603362	0.00092191

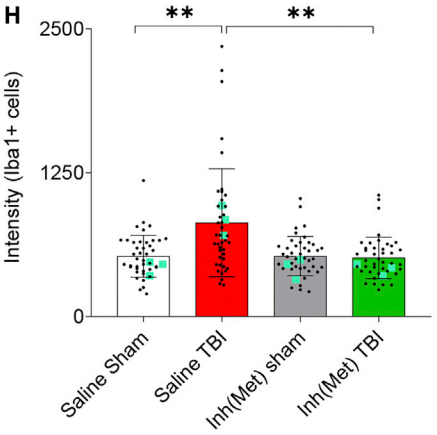

(legend on next page)

Small-molecule inhibitors of Met and VEGFR substantially alter the signaling architecture of TBI

We then explored the functional relevance of Btk, Met, and VEGFR on TBI-induced microglial activation, using small-molecule kinase inhibitors (Figure 3A). Although small molecules targeting kinases are less selective than gene-knockout manipulation, they lend themselves to explore acute effects (i.e., do not suffer from life-long target loss and unforeseen adaptation) and display translational potential. Based on the selectivity, pharmacokinetics, and blood-brain barrier penetration properties, we selected the Btk inhibitor Spebrutinib (CC-292; IC_{50} = <0.5 nM[31,32]), the Met inhibitor JNJ-38877605 (IC_{50} = 4nM[31–33]), and the broader selectivity VEGFR inhibitor Valatanib (PTK-787; inhibits VEGFR1 and VEGFR2/KDR with IC_{50} = 77 nM and 37 nM, respectively; also inhibits Flk, c-Kit, and PDGFRβ with IC_{50} = 270 nM, 730 nM, and 580 nM, respectively[34–37]).

First, we validated the target engagement of the three inhibitors (Inhs) by administering each molecule (or vehicle alone) (Inh BTK: 30 mg/kg[38], Inh Met: 40 mg/kg[32,33], Inh VEGFR: 50 mg/kg[32,35,37]) 2 h before trauma (approximately corresponding to the peak of maximum receptor occupancy, based on reported pharmacokinetic data[32,37,38]) (Figure 3A) and verified a significant decrease in pBtk (Tyr222), pMet (Tyr1234), and pVEGFR1 (Tyr1333) 3 hpi by whole-tissue western blot (Figures 3B–3D, see also Figure S3; Sal TBI vs. Sal sham: pBtk p = 0.0029, pMet p = 0.028, pVEGFR p = 0.011, Sal TBI vs. Inh TBI: pBtk p = 0.0042, pMet p = 0.0065, pVEGFR p = 0.015).

Second, we explored the large-scale signaling impact of single dose (SD) of the inhibitors of Btk (Inh(Btk) TBI, n = 4), Met (Inh(Met) TBI, n = 4) or VEGFR (Inh(VEGFR) TBI, n = 3) upon TBI (3 hpi), vs. saline-treated TBI (Sal TBI, n = 4) or sham-operated (Sal sham , n = 4) mice. PCA plots of phosphotyrosine array datasets revealed a distinct separation of groups (Figure 3E, see also Data S3). Unsupervised clustering revealed that cluster distributions for Inh(Met) TBI and Inh(VEGFR) TBI were comparable with each other, but they were significantly different from Sal TBI and Sal sham groups. On the other hand, the cluster distributions for SD Inh(Btk) TBI group was similar to the Sal TBI group. Differential phosphorylation analysis revealed 137 targets affected by an SD of Met or VEGFR inhibitors, with only 19 targets shared by the two treatments (Figure 3F). Most importantly, treatment with an SD of Met inhibitor resulted in the down-phosphorylation of microglial-specific signaling proteins Btk and Plcg2 as well as of RTKs involved in microglial activation and microgliosis such as c-Kit and IL-3R.[39,40] Comparatively, Inh(VEGFR) TBI significantly increased the phosphorylation levels of CDK5 and IGF1R responsible for microglial activation[41,42] and downregulation of immune-related IL7R/CD127, a protein associated with resting microglial phenotype[43] (Figure 3F and Data S3).

As a prerequisite of further exploration of Met regulation of microglial activation, we verified that the SD of Met inhibitor indeed significantly decreased the pMet immunoreactivity in microglia in cortical sections obtained 3 h after TBI (Figures 3G and 3H; Sal TBI vs. Sal sham: p = 0.0001, Sal TBI vs. Inh(Met)TBI: p = 0.0045).

Blockade of Met prevents the reactive microglia morphology and the induction of pro-inflammatory mediators upon TBI

We set out to characterize the impact of Met blockade on the neuroinflammatory response set in motion by TBI. First, we assessed the source of hepatocytes growth factor (HGF), the selective ligand for Met. Single-molecule *in situ* hybridization showed that HGF mRNA levels were significantly increased in both neurons and microglia after trauma. These levels, however, remained unaffected by inhibitor treatment (Figure S4A).

Next, we performed the morphometric analysis of microglial cells to evaluate morphological differences. Results revealed a retraction of processes in Sal TBI compared with sham samples (Figure 4A; coherent with reactive microglial[44,45]), whereas in the SD Inh(Met) TBI group, the size of microglia arborization was preserved (Figure 4B; branch length/cell: Sal TBI vs. Sal sham: p = 0.045, Sal TBI vs. Inh(Met) TBI: p < 0.0001, branch length/cell and endpoints/cell: Sal TBI vs. Inh(Met) TBI: p < 0.0001).

Furthermore, the TNFα mRNA (an early event in TBI[46,47]), barely detectable at baseline, was significantly upregulated upon TBI but negated by the pretreatment with the SD of Met inhibitor (Figures 4C and 4D; Sal TBI vs. Sal sham: p < 0.0001, Sal TBI vs. Inh(Met) TBI: p < 0.0001). Likewise, the M1-enriched pro-inflammatory paracrine mediator Wnt5a,[48,49] although not significantly upregulated by TBI, was dramatically suppressed by the Met inhibitor (Figures 4C and 4D; Sal TBI vs. Inh(Met) TBI: p < 0.0001). Moreover, TBI upregulated the mRNA for the complement factor C3 in neurons and microglia, but not upon pretreatment with the Met inhibitor (Figures 4E and 4F). In agreement with the reduced induction of pro-inflammatory mediators, the TBI-induced nuclear translocation of the pro-inflammatory transcription factor NF-kB in microglia[50] was suppressed by the pretreatment with the Met inhibitor (Figures 4G and 4H).

Figure 3. RTK Inhibitors treatment alters TBI signaling landscape

(A) Schematic outline of the experiment. Mice were administered with either saline or inhibitor 2 h before trauma, and samples were collected at 3 hpi.

(B–D) At 3 hpi, levels of (B) pBtk (Tyr222), (C) pMet (Tyr1235), and (D) pVEGFR1 (Tyr1333) were significantly upregulated in Sal TBI samples. Respective inhibitor treatment significantly reduced these levels to baseline. (See also Figure S3 for full scan of blots).

(E) Post-preprocessing PCA plot shows group-based clustering.

(F) List of DE proteins (p < 0.05) up-phosphorylated (red) or down-phosphorylated (blue) for comparison between Sal TBI and Inh(Met) TBI with logarithmic fold change and individual significance.

(G and H) A significant reduction in pMet expression levels was recorded upon inhibitor treatment. All graphs are represented as mean ± SD. In (B)–(D), n = 4/group. Dots indicate individual animals. Significance of differences between means were analyzed using one-way ANOVA test with Tukey correction (recommended). In (E)–(H), n = 3 for Sal sham, Inhb(Btk) TBI, and Inhb(VEGFR) TBI, and n = 4 for Sal TBI and Inhb(Met) TBI groups. Significance for DE proteins was set at p < 0.05 (BH adjusted, SD: single dose). Detailed individual comparisons are shown in Data S3. In (G)–(H), n = 4/group. In (H), small black dots indicate intensity of individual cells and green square the average per mouse. Statistical analysis was performed on the average per mouse by two-way ANOVA with Tukey correction (*p < 0.05, **p < 0.001, ***p < 0.001, ****p < 0.0001). Scale bar: 50 μm. Histograms represent average with standard deviation.

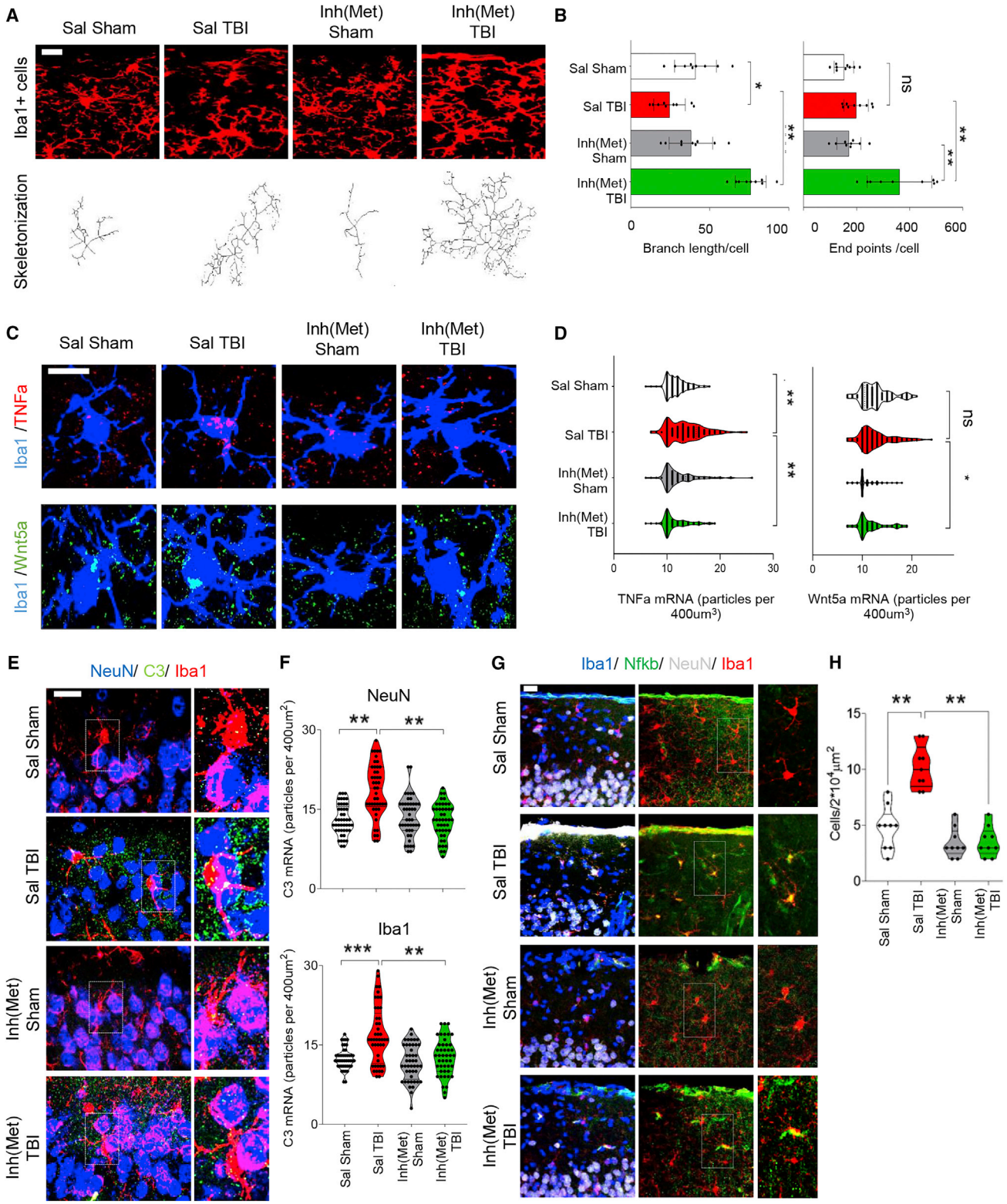

Figure 4. Acute Met blockade prevents morphological changes of microglia and induction of inflammatory mediators

(A and B) Acute morphological changes in microglia showed decreased branch length within 3 h after trauma in the Sal TBI depicting activated microglia. Single dose (SD) of Met inhibitor significantly increased a ramified or arborized microglia morphology.

(legend continued on next page)

To further characterize the reactive profile of microglia, we first demonstrated that >95% iba1+ cells were also positive for microglia marker Tmem119 across treatment groups, indicating that most Iba1+ cells are microglial cells in this condition (Figures S4B and S4C). TBI caused a substantial increase in microglia expressing upregulation of the phagocytic/lysosome marker CD68 (Iba1+/Cd68+ cells; Figures S4B and S4C) as well as the disease-associated microglia marker CD11c (Iba1+/Cd11c+ cells; Figures S4D and S4E), but both effects were negated by the pretreatment with the Met inhibitor. On the other hand, neither TBI nor Met blockade affected microglial proliferation at the considered time point (3 h) and Ki-67+ microglia cells were less than 3% in all four groups (Figures S4D and S4E).

Blockade of Met limits vascular and neuronal stress induced by TBI

We aimed at dissecting the impact of acute Met blockade on broad TBI responses. Since our model has not been fully characterized on these terms, we first determined the proteome changes occurring in the cortex at 3 h, comparing Sal TBI with sham controls only (without any inhibitor treatment). We detected a total of 6,059 proteins, among which 36 were significantly upregulated, and 25 were significantly downregulated in Sal TBI compared with Sal sham samples (Figures 5A and 5B; see also Data S4). Some of the proteins with the highest fold change (>2 fold) are involved in epigenetic responses and RNA metabolism (Hells, Syf2, Prpf38b), vascular inflammation (Itgb3, Vwa9), and brain extracellular matrix (vitronectin, Vtn).

We considered three of these proteins to monitor the impact of the SD of Met inhibitor, namely integrin beta-3 (Itgb3, an adhesion molecule expressed on endothelial cells and involved in leukocyte extravasation), lymphocyte-specific helicase (Hells, involved in epigenetic regulation and RNA processing in neurons[51]), and the vitronectin (a brain extracellular matrix protein[52,53]).

Mice were treated with an SD Met inhibitor (or saline) and subjected to TBI or sham surgery before sacrifice at 3 hpi (Figure 3A). Itgb3 was expressed at a very low level in sham-operated mice, but it was massively upregulated in endothelium upon TBI (Figure 5C; Sal TBI vs. Sal sham: 5-fold increase, $p < 0.0001$) and not in SD Inh(Met) TBI (Figure 5C; $p < 0.0001$). Hells was expressed only in neurons. Hells levels were upregulated after injury ($p < 0.0001$) but not when Met was blocked (Figure 5D; $p < 0.0001$). Vtn immunoreactivity was diffused, with clusters localized in proximity of neurons (Figure 5E). A substantial loss of Vtn was seen upon TBI ($p = 0.0001$) but not upon Met inhibition (Figure 5E; $p = 0.015$); Taken together, these data demonstrate that interference with Met activation in microglial cells produces a normalizing effect on TBI-induced responses, including vascular inflammation, neuronal stress, and matrix remodeling.

Most importantly, the Met inhibitor remained effective even when administered after the injury. In fact, phosphorylation levels of Met and Btk in microglia, as well as the levels of the neuronal Hells, were still decreased at the 3-h time point when the inhibitor was administered 30 min after the injury (Figures S5A–S5D, cf. Figures 2 and 5D).

Met blockade reduces microglial signaling and neuronal stress also in a stab wound TBI model

We sought to further validate our findings in an independent injury model using the stab wound injury (SWI) model.[54,55] Saline or inhibitor was administered 2 h before mice were subjected to a SWI, and samples were collected 3 h post injury. We opted for two prominent phosphorylation proteins; Met and Btk verified previously (cf. Figure 2). Results showed a significant increase in pMet and pBtk after SWI (Figures S6A and S6B). Interestingly, the inhibitor treatment restricted the Met as well as Btk phosphorylation. We also explored lymphocyte-specific helicase (Hells) in our second trauma model and identified a significant increase in protein levels after SWI, which was significantly reduced upon inhibitor treatment (Figure S6C, see also Figure 5D).

Both acute and prolonged Met inhibitor treatments prevent TBI-induced motor impairment

We hypothesized that blockade of acute microglial reaction by the Met inhibitor would result in beneficial outcomes at a behavioral level. Since our TBI model generates a focal lesion in correspondence of the somatosensory cortex, we exploited a quantitative test involving sensorimotor integration, based on a single pellet-reaching task. Animals were trained for 10 days to retrieve food pellets from a narrow slit using their forelimbs. Success rates were recorded before TBI and at 1, 3, 5, 7, 10, 14, 17, and 21 dpi (Figure 6A). For each animal, success and failures were quantified before and after TBI (as percentage of total attempts/trials) and defined as follows: (1) success rate (successful retrieval of the pellet), (2) failure in reaching (impairment in motor adaptation during reaching), (3) failure in grasping (impairment in digit movements), (4) failure in retrieval (digit control impairment). Animals were treated with an SD of Met/ inhibitor before TBI, followed by either daily vehicle for 7 days (Inh(Met) TBI n = 4), daily Met inhibitor (multiple doses, MD) (MD Inh(Met) TBI; n = 6), or only saline before and after the TBI (Sal TBI; n = 7). Independent groups received either an SD of Btk inhibitor (Inh(Btk) TBI; n = 3) or an SD of VEGFR inhibitor

(C and D) At 3 hpi, *in situ* hybridization showed TNFα mRNA (red) level in microglia significantly upregulated upon TBI and decreased to baseline with inhibitor treatment. Wnt5a mRNA (green) level was not affected upon TBI, but it was significantly downregulated after inhibitor treatment.
(E and F) At 3 hpi, *in situ* hybridization showed complement C3 mRNA (gray) levels significantly upregulated in neurons and microglia upon trauma. Inhibitor treatments significantly reduced C3 mRNA levels especially in Iba1+ microglial cells.
(G and H) NF-kB (Met downstream target) colocalized primarily with the Iba1+ microglia cells 3 hpi, and the effect was significantly reduced upon inhibitor treatment. In (A)–(B), n = 3/group. Two-way ANOVA test with Tukey correction (ns = not significant, *$p < 0.05$, **$p < 0.001$, ***$p < 0.001$, ****$p < 0.0001$). In (D)–(H), n = 4 animals/group. Small black dots indicate individual sections; large green dots indicate average per animals. Violin plots are used to highlight the distribution of individual cell values. Statistical analysis was performed on the average value per mouse, by two-way ANOVA test with Tukey correction. (ns = not significant, ****$p < 0.0001$). Scale bar: 50 μm. Histograms represent average with standard deviation.

A

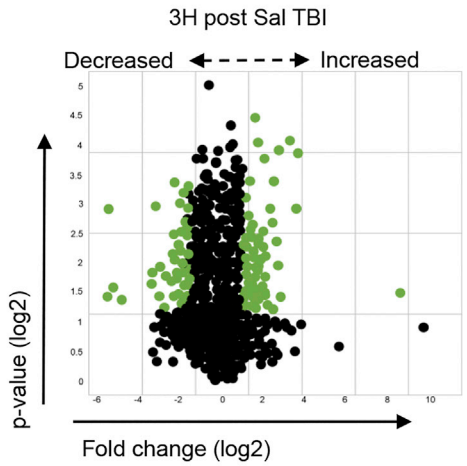

B

Protein Symbol	Ratio (TBI/Sham)	p-Value
Selenoprotein	1.82	0.0013
Actb	1.64	0.0282
Arglu1	1.67	0.0067
Papss1	1.52	0.0056
Cep55	1.53	0.0052
Lig1	1.58	0.0184
Efnb2	1.76	0.0019
Exosc7	1.76	0.0273
Fbxo44	1.63	0.0486
Fhod1	1.51	0.0173
Guca1a	1.51	0.0342
Hspb1	2.03	0.0429
Itgb3	2.59	0.0248
Ica1l	1.56	0.0051
Jsrp1	1.54	0.0323
Krt34	3.02	0.0338
Hells	7.34	0.0457
Mtr	2.18	0.0327
Apool	2.10	0.0047
Pank4	1.76	0.0063
Pgam2	1.63	0.0228
Ppcs	2.23	0.0491
Plxna3	3.46	0.0162
Prpf38b	6.29	0.0418
Syf2	2.48	0.0412
Dpy19l3	2.03	0.0398
Cnih1	2.12	0.0215
Pak4	11.11	0.0014
Rasgrp1	4.18	0.0161
Aatk	2.30	0.0293
Pak2	1.91	0.0409

Protein Symbol	Ratio (TBI/Sham)	p-Value
Mrps18b	0.31	0.0008
Cfh	0.60	0.0330
Rnf213	0.30	0.0007
G6pc3	0.37	0.0455
Mrps18b	0.31	0.0008
Cfh	0.60	0.0330
Rnf213	0.30	0.0007
G6pc3	0.37	0.0455
Krt72	0.48	0.0230
Kif5a	0.54	0.0489
Oxa1l	0.35	0.0298
Map4k2	0.29	0.0375
Ppig	0.64	0.0062
Abhd11	0.60	0.0342
Hook2	0.64	0.0383
Manbal	0.56	0.0001
Mis12	0.20	0.0005
Zwilch	0.28	0.0096
Nqo2	0.47	0.0100
Scel	0.45	0.0339
Sfxn2	0.44	0.0031
Slc24a3	0.44	0.0340
Stard7	0.64	0.0005
Tmem56	0.64	0.0217
Tmem70	0.67	0.0033
ENSMUSG000000	0.67	0.0357
Myo1g	0.63	0.0372
Vtn	0.27	0.0240
Vwa5a	0.63	0.0137
Zfp598	0.60	0.0105
Mrps18b	0.31	0.0008

C

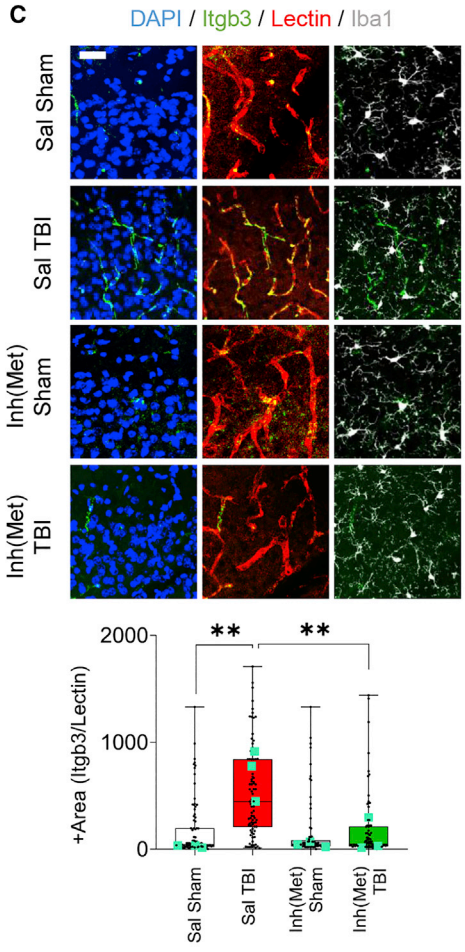

D

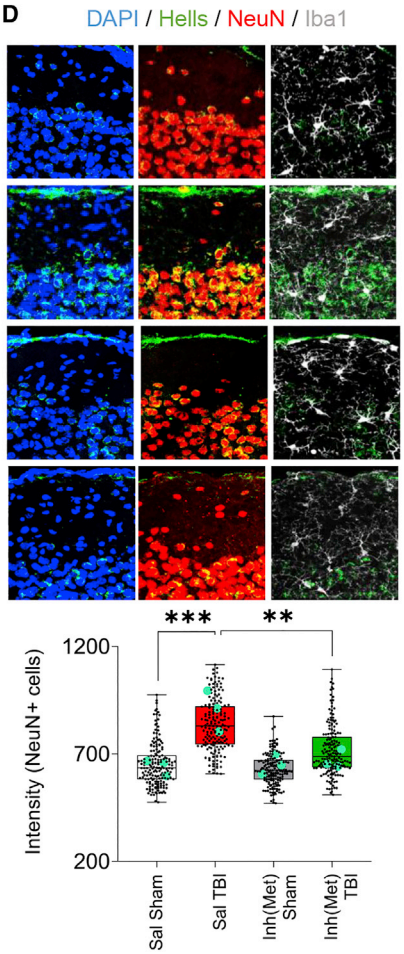

E

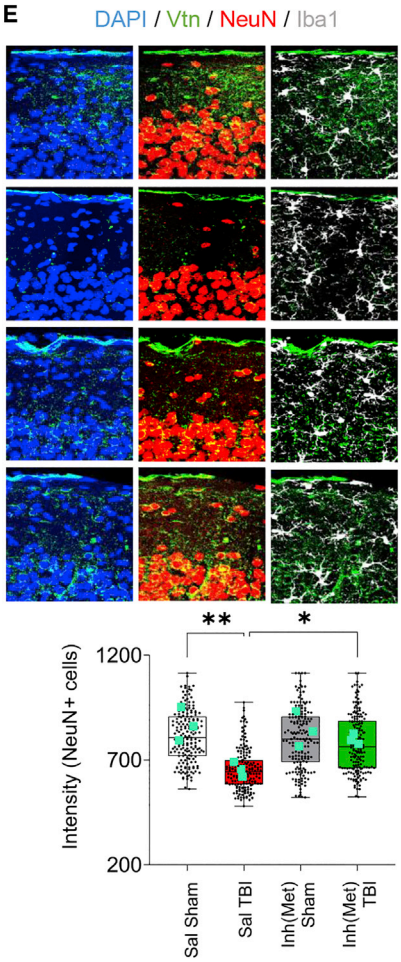

(legend on next page)

(Inh(VEGFR) TBI; n = 4) before TBI followed by daily vehicle for 7 days (Figure 6A). In Sal TBI group, the success rate significantly decreased at 1 dpi compared with pretreatment (Figure 6B; red: $p < 0.0001$ vs. pre-trauma), largely due to an increase in reaching failure rather than in grasping/retrieval failure, indicating a deficit in forelimb adaptation rather than digit control[56–58] (Figure 6B; red: $p < 0.0001$ vs. pre-trauma, Figures S7A and S7B). In the Inh(Met) TBI group (administered 2 h before TBI), a significant preservation of success rate at 1 dpi was observed (Figure 6B; green: $p = 0.0005$ vs. 1 dpi Sal TBI). Substantial beneficial effects were still seen at 2 dpi ($p = 0.0023$ vs. Sal TBI) and 3 dpi ($p = 0.0492$ vs. Sal TBI), largely due to decrease in reaching failure, (Figure 6C; green: $p = 0.048$ vs. 1 dpi Sal TBI). The Inh(VEGFR) TBI group showed a preserved performance at 1 dpi (Figures 6B and 6C; blue: $p = 0.048$ vs. 1 dpi Sal TBI) but immediately lost protective effects from 2 dpi. SD of the Btk inhibitor (Inh(Btk) TBI) failed to produce any significant effect (Figures 6B and 6C; black).

Most notably, mice that received the Met inhibitor for 7 consecutive days (MD Inh(Met) TBI; administered 2 h before trauma and daily thereafter) displayed a persistent preservation of the success rate compared with Sal TBI (Figure 6B: purple; $p < 0.0001$ vs. 1 dpi Sal TBI, $p < 0.0001$ vs. 2 dpi Sal TBI, $p = 0.0002$ vs. 3 dpi Sal TBI, $p = 0.0012$ vs. 5 dpi, $p = 0.0099$ vs. 7 dpi Sal TBI) and a significantly reduced reaching failure rate during the treatment period (between day 1 and day 7, Figure 6C: purple; $p < 0.0001$ vs. 1 dpi Sal TBI, $p = 0.0131$ vs. 2 dpi Sal TBI, $p < 0.0001$ vs. 3 dpi Sal TBI, $p = 0.012$ vs. 5 dpi Sal TBI). The improvement in success rate was fully attributed to a reduced reaching failure (Figure 6C, see also Figures S7A and S7B). Taken together, these data suggest that TBI impaired sensorimotor adaptation, while Met inhibitor treatment preserved the functioning of somatosensory networks.

Met inhibition preserves neuronal integrity and resting microglial morphology upon TBI

Finally, we explored if the beneficial effect of SD or MD of Met inhibitor on sensorimotor performance would have a counterpart on the overall neuronal loss and post-traumatic gliosis. Mice treated with either an SD or MD with a 7-day course of the Met inhibitor or with saline were sacrificed at 21 dpi (Figure 6A). In the Sal TBI, the density of NeuN+ cells was significantly reduced in the site of injury (Figures 6D and 6E; $p < 0.0001$ vs. Sal sham). Notably, an SD of Met inhibitor (Inh(Met) TBI) resulted in a significant increase in the number of surviving neurons (Figures 6D and 6E; $p < 0.0001$ vs. Sal TBI). Likewise, mice administered with Met inhibitors for 7 days (MD Inh(Met) TBI) displayed a significantly larger number of surviving NeuN+ cells in the injury area compared with saline-treated TBI mice, although still lower than sham mice (Figures 6D and 6E; $p < 0.0001$ vs. Sal TBI).

We further analyzed the density and morphology of microglial cells at this stage. SD of Met inhibitor, but not of Btk or VEGF inhibitors, displayed a significant increase in overall microglial area (a composite readout including cell number and cell size; Figure 6D, $p < 0.0001$ vs. Sal TBI). Morphometrical analysis of microglia revealed no standing difference in Sal TBI group compared with Sal sham controls but a statistically significant increase in branch length and number of end points per cell in both SD and MD Met inhibitor treated groups (Figures S7C and S7D; Inh(Met) TBI vs Sal TBI; branch length $p < 0.0001$, endpoint $p < 0.027$; MD Inh(Met) TBI vs Sal TBI; branch length $p < 0.01$, endpoint $p < 0.001$). An SD of Btk inhibitor (Inh(Btk) TBI) or VEGFR inhibitor (Inh(VEGFR) TBI) displayed no effect on morphometrical readouts. Taken together the results suggest that Met inhibitor treatment results in an improved protection of neuronal integrity and increases the preservation of a ramified state.

HGF levels are acutely upregulated in the CSF of human TBI patients

Our murine data collectively demonstrated the role of Met signaling in driving the acute reactivity of microglia upon TBI. The ligand for Met, HGF, is a soluble mediator released by multiple cell types and normally found in the extracellular space[59] upon cleavage of the membrane-bound precursor.[60] It is known to be detectable in the cerebrospinal fluid (CSF).[61] We sought to validate the relevance of the HGF/Met axis in human neurotrauma patients (clinical and demographic data in Table S5) by assessing the levels of HGF in the CSF. Compared with two cohorts of non-traumatic CSF controls (older patients with normal pressure hydrocephalus-control, cohort 1, and younger patients with tension-type headache-control, cohort 2), HGF levels were very strongly increased already at D0, partially declined at D1, and returned to values closer to the baseline by D3 in CSF of TBI patients (Figure 7A). In a subset of patients that were longitudinally sampled, a similar trend was observed, with massive elevation in the early hours and quick decline toward the baseline (Figure 7B). In order to compare the time course of HGF, we measured the levels of two other pro-inflammatory cytokines, IL-6 and IL1β, known to increase in acute (IL-6) or sub-acute

Figure 5. Met inhibitor prevents neuronal stress, vascular inflammation, and brain matrix degradation upon TBI

(A) Post-proteome analysis volcano plot showing distribution of proteins of the injured cortex compared with Sal sham at 3 hpi.

(B) List of statistically significant upregulated (red) and downregulated (blue) proteins with fold change and individual significance (detailed individual comparisons are shown in Data S4).

(C) Integrin beta 3 (itgb3) colocalized with vascular marker (lectin) and limited to no colocalization with neurons (NeuN+) or microglia (Iba1+). Itgb3 levels (Itgb3+ area against total vessel length) were significantly upregulated at 3 hpi and reduced to baseline levels with inhibitor treatment.

(D) Lymphoid-specific helicase (Hells) colocalized with neurons (NeuN+) and showed no overlapping with microglia (Iba1+) cells.

(E) Vitronectin (Vtn) colocalized with neurons (NeuN+) and showed no overlapping with microglia (Iba1+) cells. Vtn levels were significantly downregulated after TBI, and single-dose Met inhibitor treatment restored Vtn levels to baseline levels. Boxplots represent 25th–75th percentile (whiskers represent range). Small black dots indicate individual sections; large green dots indicate average per animal. In (A)–(B), n = 3/group. Significance for DE proteins was set at $p < 0.05$ (FDR adjusted). In (C)–(E), n = 4/group. Dots in graphs indicate individual cells/vessels. In (C), expression levels were normalized over the total length of the vessel. Statistical analysis was performed on the average value per mouse by two-way ANOVA with Tukey correction. (*$p < 0.05$, **$p < 0.001$, ***$p < 0.001$, ****$p < 0.0001$). Scale bar: 200 μm. Boxplots display the 25–75 percentile interval (box contours) and the full range (whiskers).

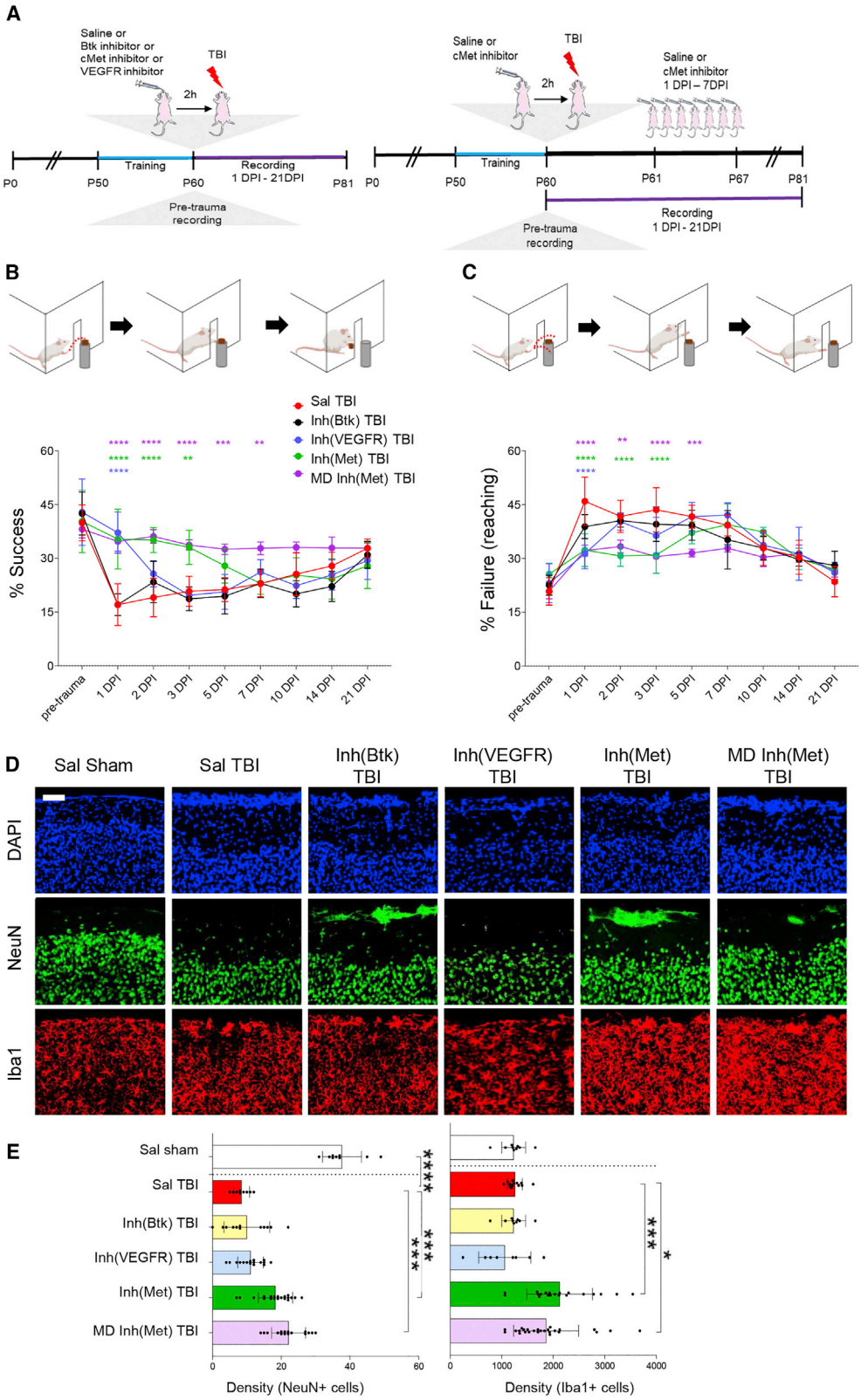

(legend on next page)

(IL1β) phases.[62,63] Levels of IL1β showed a positive trend increasing from D0 to D3 (Figures 7C and 7D). On the other hand, IL6 levels were elevated at D0 and quickly declined over the next 3 days (Figures 7E and 7F). Thus, HGF trend was similar to that of IL6 and differed from IL1β. In fact, HGF levels were strongly correlated with IL6 levels in each sample. Thus, HGF up-regulation characterizes the acute phases of human TBI, in agreement with what is observed in murine samples.

DISCUSSION

TBI is characterized by the sudden and simultaneous unfolding of neuronal, glial, and vascular responses to injury, which involves multiple signaling cascades setting in motion, cell death, local inflammation, synapse disruption, glial activation, and blood-brain barrier disruption. We have captured the complexity of these events initially by monitoring the phosphorylation status of 39 different RTKs at multiple timepoints after TBI. This approach has the advantage of focusing on multiple targets with high translational potential (tyrosine kinases) while identifying the signature of several concomitant processes and cell subtypes.

Our findings confirm previous anecdotal reports about individual RTKs[14,64,65] and further extend the characterization of the acute signaling landscape in TBI. Notably, the 3 hpi and 1 dpi samples displayed changes in the phosphorylation of a set of receptors involved in microglial reactivity, namely the upregulation of the phosphorylation of pro-inflammatory Met and MSPR, together with the concomitant downregulation in the phosphorylation of reactive microglia-suppressing[4,19] Axl and Dtk (Figures 1C and 1D), pointing toward a coordinated shift in the balance between different signals regulating microglial activation. Notably, this effect is not present for milder TBI (where Axl and Dtk are actually up-phosphorylated), indicating that even small differences in TBI severity may translate in either the enhancement or the suppression of the reactive microglial phenotype (Figure S1H).

Further characterization of the signaling landscape at 3 hpi using a distinct array platform and immunohistochemistry not only confirmed several of the targets already identified (most notably Met, VEGFR1, and EGFR) but revealed the phosphorylation of RTKs such as Flt3[66] and a series of NRTKs such as Fer, Lck, Abl, and Btk involved in microglia reactivity and neuroinflammation. The latter is largely restricted to immune cells, including microglia. We elected to use small-molecule inhibitors to explore the roles of Met, VEGFR, and Btk on microglial activation and on the overall secondary damage. Both the Met inhibitor and the VEGFR inhibitor exerted a substantial impact on the phosphoproteome. The Met inhibitor caused the down-phosphorylation of a number of RTKs involved in immune function (c-Kit, IL3R, PDGFRa) and of related signaling molecules, most notably Btk and Hrs (the hepatocyte growth factor-regulated tyrosine kinase substrate), a critical signaling hub for Met.[67,68] The VEGFR inhibitor affected a much larger set of targets, coherently with the broader expression of the receptor and the broader specificity of the inhibitor. Interestingly, the VEGFR inhibitor affected targets partially overlapped with the Met targets, in particular with the down-phosphorylation of Btk, Hrs, IL3R, and EGFR. The Btk inhibitor itself does not appear to be sufficient to bring about a significant change in the phospho-proteome or a beneficial effect in histological and behavioral readouts. This finding is in contrast with the previously established beneficial effect of Btk suppression in stroke[69] and in demyelinating disease.[70] Indeed, the limited effect of the Btk inhibitor on the signaling cascades, despite an impact on Btk phosphorylation itself, suggests that either the redundancy of the signaling cascades is so that inhibition of a single downstream/non-receptor kinase is less effective than the inhibition of upstream receptors or that a more intense suppression of Btk is needed to observe beneficial effects. The pan VEGFR inhibitor also delivered no beneficial effect on behavior. It may be speculated that the broader selectivity (including VEGFRs, PDGFRs, c-kit, and others[34]) may have led to the interference with multiple pathophysiological cascades, either beneficial or detrimental, with no net beneficial effect.

We have mechanistically investigated the role of Met blockade on microglial activation (and its broad consequences in the acute TBI landscape). We demonstrated that the reactive morphology and the induction of inflammatory mediators in microglia upon TBI are prevented by Met blockade and that vascular inflammation, extracellular matrix degradation, and neuronal stress are also prevented. Finally, the grasping task revealed that either an SD or a 7-day MD treatment with Met inhibitor delivered a significant improvement in motor performance, corresponding to an enhanced preservation of neuronal integrity in the site of injury.

Taken together, our dataset identified Met as a new regulator of microglial activation and, more broadly, of the neuroimmunological response to TBI. Met and the closely related RON receptor are expressed in microglia,[26,71–73] macrophages,[74,75] and other immune cells including subsets of B and T lymphocytes,[76,77] as well as in a number of non-neuronal tissues.[78] In

Figure 6. Met inhibitor improves TBI-induced motor impairment and preserves neuronal density and branched microglial morphology

(A) Schematic outline of the experiment.

(B) Success rate was significantly reduced at 1 dpi until 14 dpi (Sal TBI group, red; Inh(Btk) TBI, black) compared with respective pre-treatments. Success percentage of two groups, Inh(Met) TBI, green, and Inh(VEGFR) TBI, blue, was significantly improved compared with Sal TBI. Inh(Met) TBI showed a persistent improvement in success percentage until 3 dpi compared with Sal TBI. Success percentage was significantly improved with consecutive multiple doses of Met treatment: MD Inh(Btk) TBI, purple, starting 1 dpi with persistent improvement until 7 dpi.

(C) Significant increase was reported in reaching failure in Sal TBI compared with pre-trauma and Inh(Btk) TBI at 1 dpi. A significant decrease in reaching failure was observed in Inh(Met) TBI and Inh(VEGFR) TBI compared with Sal TBI. Inh(Met) TBI showed a persistent decrease in reaching failure until 3 dpi compared with Sal TBI. MD Inh(Met) TBI group showed a significant decrease in the percentage of reaching failure compared with Sal TBI from 1 dpi until 5 dpi.

(D and E) Reduced neuronal count was observed in Sal TBI group compared with Sal sham, and neuroprotection was observed in Inh(Met) TBI and MD Inh(Met) compared with Sal TBI. Microglia cells also showed an increase in density among Inh(Met) TBI and MD Inh(Met) TBI. All graphs are represented as mean ± SD. In (A)–(C), n = 7 for Sal TBI, n = 3 for Inh(Btk) TBI, n = 4 for Inh(VEGFR) TBI and Inh(Met) TBI, and n = 6 for MD Inh(Met) TBI. Two-way ANOVA test with Tukey correction. (*$p < 0.05$, **$p < 0.001$, ***$p < 0.001$, ****$p < 0.0001$). Scale bar: 300 μm. Histograms and timecourse plots represent average with standard deviation.

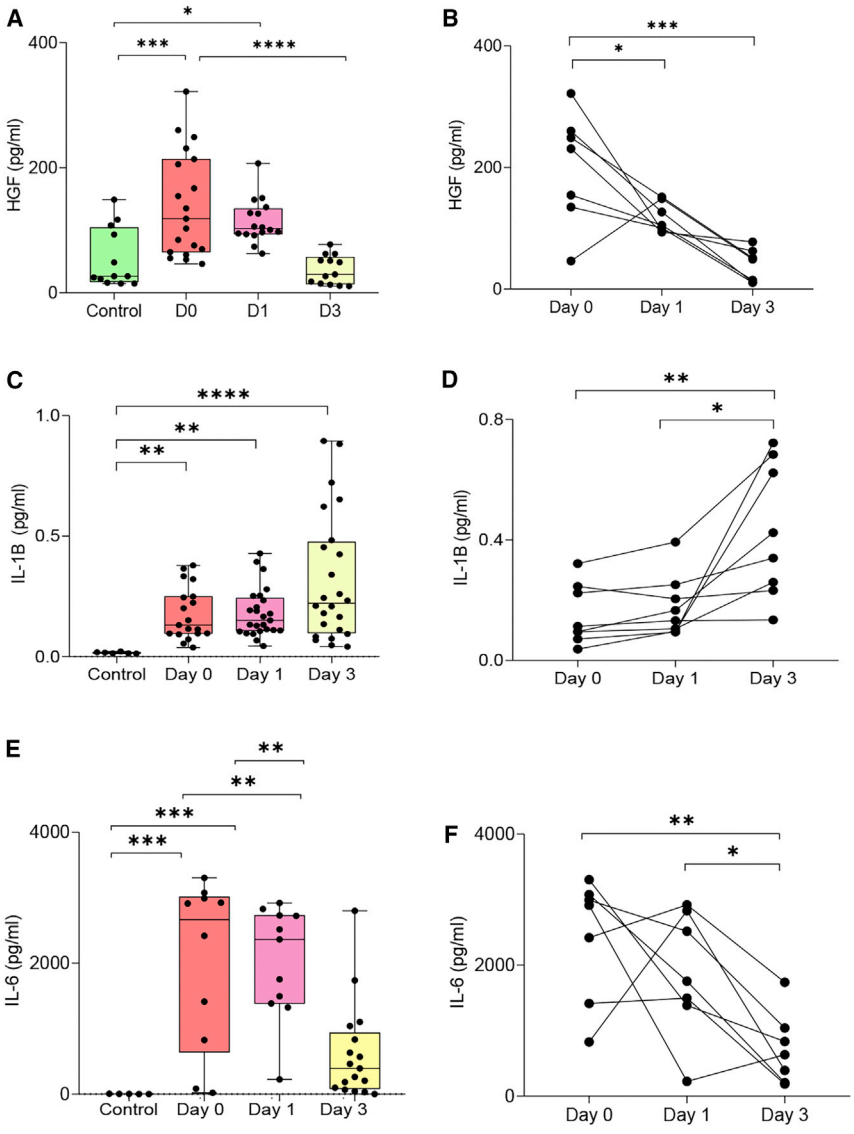

Figure 7. HGF is upregulated in the CSF of human TBI patients

(A–E) Significant upregulation of (A–B) HGF, (C–D) IL1β, and (E–F) IL6 protein in cerebrospinal fluid (CSF) samples of traumatic brain injury patients compared with control samples. ELISA results for (B) HGF and SIMOA results for (F) IL6 show upregulation at 0 and 1 day after trauma and reduce after 3 days. On the other hand, (D) IL1β levels increase over time from day 0 to day 3. Boxplots represent the 25th–75th percentile and median value (whiskers represent range). In (A), (C), and (E), n = 13 for control, n = 18 for day 0, n = 25 for day 1, n = 28 for day 3. In (B), (D), and (E), n = 7 for all groups. Dots represent individual human CSF samples. Clinico-demographic details are reported in Table S5. Two-way ANOVA test with Tukey correction. (*p < 0.05, **p < 0.001, ***p < 0.001, ****p < 0.0001). Boxplots display the 25–75 percentile interval (box contours) and the full range (whiskers).

macrophages, Met induces motility, chemotaxis and chemokine secretion,[75,79] and proliferation.[25] Interestingly, Met has been reported to shift macrophage polarization toward the so-called non-inflammatory M2 phenotype,[74,80] and it stimulates IL10 secretion.[81] On the other hand, Met activation enhances macrophages infiltration and chemokine secretion[79,82] to drive the proliferation of M1-polarized macrophages,[25] proposing that Met effects may be dependent on the local microenvironment. While microglia express both Met and its ligand HGF,[73] the consequences of Met signaling in microglia in a pathology context are unclear. Our data suggest that Met activation may gate the induction of a reactive phenotype and contribute to the induction of inflammatory cytokines. Additional mechanisms may be involved in the overall effect of Met inhibition on microglia. We have also shown that Met inhibition prevents the nuclear translocation of NF-kB, which is a key regulator of the reactive microglia state and phagocytes.[50] Given the role in inducing chemotaxis, Met may contribute (together with other chemotactic factors[5]) to microglial migration toward the site of injury. Interestingly, microglial cells remained in a ramified-morphology state up to 14 days after the last administration of the inhibitor, suggesting that Met may permanently prevent access to a reactive phenotype. Interestingly, a similar phenotype of increased microglial arborization (“hyper-ramified microglia”) has been previously reported,[83–86] in particular upon traumatic injury.[45] The characterization of this morphologically distinct microglia state remains not univocal. It has been reported that hyper-ramified microglia do not show classical signs of reactive or detrimental microglia[85] and may rather be associated with increased activity of neuronal circuits.[87]

Our findings identify a number of RTKs with transient activation in the early phases of the TBI responses. Met inhibition shows that interventions at this stage may have profound acute as well as long-lasting modulatory effects on microglial response to TBI, neuronal integrity, and motor performance. Thus, Met provides a proof of concept for the identification of new modulators of TBI response based on their impact on the acute large-scale signaling landscape, which may shape the overall response to trauma in the long term.

Limitations of the study

The present study is not without limitations. First, our exploration of the role of Met, VEGFR, and Btk relies on small-molecule inhibitors. This approach has the advantages to explore selectively acute effects, devoid of long-term or developmental adaptations due to constitutive gene knockout and, at the same time, to provide insights toward drug repurposing strategy (therefore

delivering a better translational outlook). On the other hand, small-molecule TK inhibitors are rarely completely selective, and inhibition of closely related RTK (e.g., simultaneous blockade of VEGFR1, VEGFR2, and VEGFR3) may contribute to the overall effect. Moreover, the efficacy of small-molecule inhibitors is affected by their pharmacokinetics, in particular by their blood-brain barrier penetration, so we have provided proof of target engagement. Second, we elected to investigate a TBI model with relatively mild (in terms of NSS score and histology) consequences, and the findings may be not directly extrapolated to conditions characterized by large hematomas, extensive necrotic lesions, or bone fracture. In fact, even a small difference in kinetic energy may drive distinctive responses (as shown in this paper), and hematomas may drive substantially different biology.[14] Additional variables to be considered in the exploration of the parametric space would include sex, age, genetic background, and comorbidities besides the severity of injury. Having provided a proof of concept in the present work, additional variables may be tested in future. Third, the elevation of HGF seen in a clinically representative cohort of human subjects suggests that our experimental findings may be applied to human subjects. The study of CSF samples is subject to the heterogeneity associated with clinical studies. Furthermore, since ventricular CSF samples from healthy subjects cannot be obtained for ethical reasons, the reference cohorts are not perfectly matched for age (control ventricular CSF samples are older than TBI patients) or for anatomical site (lumbar samples from tension-type headache patients is not a precise match for ventricular CSF). Nevertheless, the magnitude of the effect of TBI appears to be larger than any variability associated with age or with site of sampling.

STAR★METHODS

Detailed methods are provided in the online version of this paper and include the following:

- KEY RESOURCES TABLE
- RESOURCE AVAILABILITY
  - Lead contact
  - Materials availability
  - Data and code availability
- EXPERIMENTAL MODEL AND SUBJECT DETAILS
  - Mouse strains
  - Human CSF samples
  - Traumatic brain injury (TBI) model
  - Stab wound injury (SWI) model
- METHOD DETAILS
  - Antibodies
  - Perfusions and tissue processing
  - Protein extraction
  - Phospho RTK array processing
  - Tyrosine kinase array processing
  - Proteomics (mass spectrometry) measurement and analysis
  - Pharmacological agents and treatment procedures
  - Immunostaining
  - Western blotting
  - Microscopy
  - Behavioral performance and assessment
  - *In situ* hybridization
  - ELISA and SIMOA assays
- QUANTITATIVE AND STATISTICAL ANALYSIS
  - Array analysis
  - Image analysis
  - Statistical analysis
- ADDITIONAL RESOURCES

SUPPLEMENTAL INFORMATION

Supplemental information can be found online at https://doi.org/10.1016/j.celrep.2022.111867.

ACKNOWLEDGMENTS

The present work has been supported by the ERANET-NEURON initiative. F.R., M.G., A.T., M.M., J.K., and R.R. are members of the MICRONET consortium (funded by BMBF: FKZ 01EW1705A for F.R.). M.G. is independently funded by the TRR274. M.M. is supported by FWO as part of the MICRONET consortium in the ERANET-NEURON initiative grant awarded to A.T. (G0H1817N). R.R. is also independently funded by the Hannelore Kohl Foundation Award. F.R. is also funded by DFG in the context of the SFB1149 (DFG No. 251293561) as well as through individual grants (DFG No. 443642953, 431995586, and 446067541).

AUTHOR CONTRIBUTIONS

F.R. conceived the study and supervised the project. R.R. and F.R. planned the experiments. R.R. and M.E.W. performed R software-based analyses. R.R. and M.M. performed the behavior experiments. R.R., M.M., and L.E. analyzed the behavioral data. S.M.H., M.G., and J.K. performed and analyzed the proteomic experiments. A.C. and M.M.K. collected the human CSF samples. R.R. and S.S.K. performed the analysis of the human CSF. R.R., F.o.H., and A.C. performed the trauma surgery and collected the samples for histological analysis. R.R. prepared figures and drafted the manuscript. F.R., A.T., M.G., T.B., A.L., M.M.K., and R.R. authors contributed to the final version of the manuscript. All authors read and approved the manuscript.

DECLARATION OF INTERESTS

There is no conflict of interest among the authors.

Received: January 26, 2022
Revised: October 17, 2022
Accepted: November 30, 2022
Published: December 27, 2022

REFERENCES

1. Alam, A., Thelin, E.P., Tajsic, T., Khan, D.Z., Khellaf, A., Patani, R., and Helmy, A. (2020). Cellular infiltration in traumatic brain injury. In J. Neuroinflammation, *17* (BioMed Central Ltd). https://doi.org/10.1186/s12974-020-02005-x.
2. Davalos, D., Grutzendler, J., Yang, G., Kim, J.V., Zuo, Y., Jung, S., Littman, D.R., Dustin, M.L., and Gan, W.B. (2005). ATP mediates rapid microglial response to local brain injury in vivo. Nat. Neurosci. *8*, 752–758. https://doi.org/10.1038/nn1472.
3. Jassam, Y.N., Izzy, S., Whalen, M., McGavern, D.B., and El Khoury, J. (2017). Neuroimmunology of traumatic brain injury: time for a paradigm shift. Neuron *95*, 1246–1265. https://doi.org/10.1016/j.neuron.2017.07.010.
4. Fourgeaud, L., Través, P.G., Tufail, Y., Leal-Bailey, H., Lew, E.D., Burrola, P.G., Callaway, P., Zagórska, A., Rothlin, C.V., Nimmerjahn, A., and

Lemke, G. (2016). TAM receptors regulate multiple features of microglial physiology. Nature *532*, 240–244. https://doi.org/10.1038/nature17630.

5. Roth, T.L., Nayak, D., Atanasijevic, T., Koretsky, A.P., Latour, L.L., and McGavern, D.B. (2014). Transcranial amelioration of inflammation and cell death after brain injury. Nature *505*, 223–228. https://doi.org/10.1038/nature12808.
6. Nimmerjahn, A., Kirchhoff, F., and Helmchen, F. (2005). Resting microglial cells are highly dynamic surveillants of brain parenchyma in vivo. Science *308*, 1314–1318. https://doi.org/10.1126/science.1110647.
7. Ritzel, R.M., He, J., Li, Y., Cao, T., Khan, N., Shim, B., Sabirzhanov, B., Aubrecht, T., Stoica, B.A., Faden, A.I., et al. (2021). Proton extrusion during oxidative burst in microglia exacerbates pathological acidosis following traumatic brain injury. Glia *69*, 746–764. https://doi.org/10.1002/glia.23926.
8. Ma, M.W., Wang, J., Dhandapani, K.M., Wang, R., and Brann, D.W. (2018). NADPH oxidases in traumatic brain injury – promising therapeutic targets? Redox Biol. *16*, 285–293. https://doi.org/10.1016/j.redox.2018.03.005.
9. Zhang, J., Malik, A., Choi, H.B., Ko, R.W.Y., Dissing-Olesen, L., and MacVicar, B.A. (2014). Microglial CR3 activation triggers long-term synaptic depression in the hippocampus via NADPH oxidase. Neuron *82*, 195–207. https://doi.org/10.1016/j.neuron.2014.01.043.
10. Wang, C.F., Zhao, C.C., Liu, W.L., Huang, X.J., Deng, Y.F., Jiang, J.Y., and Li, W.P. (2020). Depletion of microglia attenuates dendritic spine loss and neuronal apoptosis in the acute stage of moderate traumatic brain injury in mice. J. Neurotrauma *37*, 43–54. https://doi.org/10.1089/neu.2019.6460.
11. Herzog, C., Pons Garcia, L., Keatinge, M., Greenald, D., Moritz, C., Peri, F., and Herrgen, L. (2019). Rapid clearance of cellular debris by microglia limits secondary neuronal cell death after brain injury in vivo. Development (Camb.) *146*, dev174698. https://doi.org/10.1242/dev.174698.
12. Willis, E.F., MacDonald, K.P.A., Nguyen, Q.H., Garrido, A.L., Gillespie, E.R., Harley, S.B.R., Bartlett, P.F., Schroder, W.A., Yates, A.G., Anthony, D.C., et al. (2020). Repopulating microglia promote brain repair in an IL-6-dependent manner. Cell *180*, 833–846.e16. https://doi.org/10.1016/j.cell.2020.02.013.
13. Wicher, G., Wallenquist, U., Lei, Y., Enoksson, M., Li, X., Fuchs, B., Abu Hamdeh, S., Marklund, N., Hillered, L., Nilsson, G., and Forsberg-Nilsson, K. (2017). Interleukin-33 promotes recruitment of microglia/macrophages in response to traumatic brain injury. J. Neurotrauma *34*, 3173–3182. https://doi.org/10.1089/neu.2016.4900.
14. Chandrasekar, A., Olde Heuvel, F., Wepler, M., Rehman, R., Palmer, A., Catanese, A., Linkus, B., Ludolph, A., Boeckers, T., Huber-Lang, M., et al. (2018). The neuroprotective effect of ethanol intoxication in traumatic brain injury is associated with the suppression of ERBB signaling in parvalbumin-positive interneurons. J. Neurotrauma *35*, 2718–2735. https://doi.org/10.1089/neu.2017.5270.
15. Roselli, F., Chandrasekar, A., and Morganti-Kossmann, M.C. (2018). Interferons in traumatic brain and spinal cord injury: current evidence for translational application. In Front. Neurol., *9* (Frontiers Media S.A), p. 458. https://doi.org/10.3389/fneur.2018.00458.
16. Bai, L., Bai, G., Wang, S., Yang, X., Gan, S., Jia, X., Yin, B., and Yan, Z. (2020). Strategic white matter injury associated with long-term information processing speed deficits in mild traumatic brain injury. Hum. Brain Mapp. *41*, 4431–4441. https://doi.org/10.1002/hbm.25135.
17. Tondo, G., Perani, D., and Comi, C. (2019). TAM receptor pathways at the crossroads of neuroinflammation and neurodegeneration. Dis. Markers *2019*, 2387614. https://doi.org/10.1155/2019/2387614.
18. Zeisel, A., Muñoz-Manchado, A.B., Codeluppi, S., Lönnerberg, P., La Manno, G., Juréus, A., Marques, S., Munguba, H., He, L., Betsholtz, C., et al. (2015). Cell types in the mouse cortex and hippocampus revealed by single-cell RNA-seq. Science *347*, 1138–1142. https://doi.org/10.1126/science.aaa1934.
19. Ray, A.K., DuBois, J.C., Gruber, R.C., Guzik, H.M., Gulinello, M.E., Perumal, G., Raine, C., Kozakiewicz, L., Williamson, J., and Shafit-Zagardo, B. (2017). Loss of Gas6 and Axl signaling results in extensive axonal damage, motor deficits, prolonged neuroinflammation, and less remyelination following cuprizone exposure. Glia *65*, 2051–2069. https://doi.org/10.1002/glia.23214.
20. Elmore, M.R.P., Najafi, A.R., Koike, M.A., Dagher, N.N., Spangenberg, E.E., Rice, R.A., Kitazawa, M., Matusow, B., Nguyen, H., West, B.L., and Green, K.N. (2014). Colony-stimulating factor 1 receptor signaling is necessary for microglia viability, unmasking a microglia progenitor cell in the adult brain. Neuron *82*, 380–397. https://doi.org/10.1016/j.neuron.2014.02.040.
21. Li, S., Hu, X., Doycheva, D.M., Huang, L., Lenahan, C., Liu, R., Huang, J., Xie, S., Tang, J., Zuo, G., et al. (2020). Rh-CSF1 attenuates neuroinflammation via the CSF1R/PLCG2/PKCε pathway in a rat model of neonatal HIE. J. Neuroinflammation *17*, 182. https://doi.org/10.1186/s12974-020-01862-w.
22. Wu, S.Y., Pan, B.S., Tsai, S.F., Chiang, Y.T., Huang, B.M., Mo, F.E., and Kuo, Y.M. (2020). BDNF reverses aging-related microglial activation. J. Neuroinflammation *17*, 210. https://doi.org/10.1186/s12974-020-01887-1.
23. Huang, L., Jiang, S., and Shi, Y. (2020). Tyrosine kinase inhibitors for solid tumors in the past 20 years (2001–2020) Journal of Hematology and Oncology*13*, p. 143, Issue 1. https://doi.org/10.1186/s13045-020-00977-0.
24. Terashima, T., Nakae, Y., Katagi, M., Okano, J., Suzuki, Y., and Kojima, H. (2018). Stem cell factor induces polarization of microglia to the neuroprotective phenotype in vitro. Heliyon *4*, e00837. https://doi.org/10.1016/j.heliyon.2018.e00837.
25. Moransard, M., Sawitzky, M., Fontana, A., and Suter, T. (2010). Expression of the HGF receptor c-met by macrophages in experimental autoimmune encephalomyelitis. Glia *58*, 559–571. https://doi.org/10.1002/glia.20945.
26. Di Renzo, M.F., Bertolotto, A., Olivero, M., Putzolu, P., Crepaldi, T., Schiffer, D., Pagni, C.A., and Comoglio, P.M. (1993). Selective expression of the Met/HGF receptor in human central nervous system microglia. Oncogene *8*, 219–222. https://europepmc.org/article/med/8380919.
27. Nam, H.Y., Nam, J.H., Yoon, G., Lee, J.Y., Nam, Y., Kang, H.J., Cho, H.J., Kim, J., and Hoe, H.S. (2018). Ibrutinib suppresses LPS-induced neuroinflammatory responses in BV2 microglial cells and wild-type mice. J. Neuroinflammation *15*, 271. https://doi.org/10.1186/s12974-018-1308-0.
28. Shah, V.B., Ozment-Skelton, T.R., Williams, D.L., and Keshvara, L. (2009). Vav1 and PI3K are required for phagocytosis of β-glucan and subsequent superoxide generation by microglia. Mol. Immunol. *46*, 1845–1853. https://doi.org/10.1016/j.molimm.2009.01.014.
29. Sierksma, A., Lu, A., Mancuso, R., Fattorelli, N., Thrupp, N., Salta, E., Zoco, J., Blum, D., Buée, L., De Strooper, B., and Fiers, M. (2020). Novel Alzheimer risk genes determine the microglia response to amyloid-β but not to TAU pathology. EMBO Mol. Med. *12*, e10606. https://doi.org/10.15252/emmm.201910606.
30. Suh, H.-S., Kim, M.-O., and Lee, S.C. (2005). Inhibition of granulocyte-macrophage colony-stimulating factor signaling and microglial proliferation by anti-CD45RO: role of Hck tyrosine kinase and phosphatidylinositol 3-kinase/akt. J. Immunol. *174*, 2712–2719. https://doi.org/10.4049/jimmunol.174.5.2712.
31. Etnyre, D., Stone, A.L., Fong, J.T., Jacobs, R.J., Uppada, S.B., Botting, G.M., Rajanna, S., Moravec, D.N., Shambannagari, M.R., Crees, Z., et al. (2014). Targeting c-Met in melanoma: mechanism of resistance and efficacy of novel combinatorial inhibitor therapy. Cancer Biol. Ther. *15*, 1129–1141. https://doi.org/10.4161/cbt.29451.
32. Lolkema, M.P., Bohets, H.H., Arkenau, H.T., Lampo, A., Barale, E., De Jonge, M.J.A., Van Doorn, L., Hellemans, P., De Bono, J.S., and Eskens,

F.A.L.M. (2015). The c-Met tyrosine kinase inhibitor JNJ-38877605 causes renal toxicity through species-specific insoluble metabolite formation. Clin. Cancer Res. *21*, 2297–2304. https://doi.org/10.1158/1078-0432.CCR-14-3258.

33. De Bacco, F., D'Ambrosio, A., Casanova, E., Orzan, F., Neggia, R., Albano, R., Verginelli, F., Cominelli, M., Poliani, P.L., Luraghi, P., et al. (2016). MET inhibition overcomes radiation resistance of glioblastoma stem-like cells. EMBO Mol. Med. *8*, 550–568. https://doi.org/10.15252/emmm.201505890.

34. Wood, J.M., Bold, G., Buchdunger, E., Cozens, R., Ferrari, S., Frei, J., Hofmann, F., Mestan, J., Mett, H., O'Reilly, T., et al. (2000). PTK787/ZK 222584, a novel and potent inhibitor of vascular endothelial growth factor receptor tyrosine kinases, impairs vascular endothelial growth factor-induced responses and tumor growth after oral administration. Cancer Res. *60*, 2178–2189. https://cancerres.aacrjournals.org/content/60/8/2178.short.

35. Kong, L.J., Li, H., Du, Y.J., Pei, F.H., Hu, Y., Zhao, L.L., and Chen, J. (2017). Vatalanib, a tyrosine kinase inhibitor, decreases hepatic fbrosis and sinusoidal capillarization in CCl4-induced fbrotic mice. Mol. Med. Rep. *15*, 2604–2610. https://doi.org/10.3892/mmr.2017.6325.

36. Shankar, A., Borin, T.F., Iskander, A., Varma, N.R., Achyut, B.R., Jain, M., Mikkelsen, T., Guo, A.M., Chwang, W.B., Ewing, J.R., et al. (2016). Combination of vatalanib and a 20-HETE synthesis inhibitor results in decreased tumor growth in an animal model of human glioma. OncoTargets Ther. *9*, 1205–1219. https://doi.org/10.2147/OTT.S93790.

37. Reardon, D.A., Egorin, M.J., Desjardins, A., Vredenburgh, J.J., Beumer, J.H., Lagattuta, T.F., Gururangan, S., Herndon, J.E., Salvado, A.J., and Friedman, H.S. (2009). Phase I pharmacokinetic study of the vascular endothelial growth factor receptor tyrosine kinase inhibitor vatalanib (PTK787) plus imatinib and hydroxyurea for malignant glioma. Cancer *115*, 2188–2198. https://doi.org/10.1002/cncr.24213.

38. Evans, E.K., Tester, R., Aslanian, S., Karp, R., Sheets, M., Labenski, M.T., Witowski, S.R., Lounsbury, H., Chaturvedi, P., Mazdiyasni, H., et al. (2013). Inhibition of Btk with CC-292 provides early pharmacodynamic assessment of activity in mice and humans. J. Pharmacol. Exp. Therapeut. *346*, 219–228. https://doi.org/10.1124/jpet.113.203489.

39. Natarajan, C., Sriram, S., Muthian, G., and Bright, J.J. (2004). Signaling through JAK2-STAT5 pathway is essential for IL-3-induced activation of microglia. Glia *45*, 188–196. https://doi.org/10.1002/glia.10316.

40. Spiller, K.J., Restrepo, C.R., Khan, T., Dominique, M.A., Fang, T.C., Canter, R.G., et al. (2018). Microglia-mediated recovery from ALS-relevant motor neuron degeneration in a mouse model of TDP-43 proteinopathy. Nat. Neurosci. *21*, 329–340. https://doi.org/10.1038/s41593-018-0083-7.

41. Muyllaert, D., Terwel, D., Kremer, A., Sennvik, K., Borghgraef, P., Devijver, H., Dewachter, I., and Van Leuven, F. (2008). Neurodegeneration and neuroinflammation in cdk5/p25-inducible mice: a model for hippocampal sclerosis and neocortical degeneration. Am. J. Pathol. *172*, 470–485. https://doi.org/10.2353/ajpath.2008.070693.

42. O'Donnell, S.L., Frederick, T.J., Krady, J.K., Vannucci, S.J., and Wood, T.L. (2002). IGF-I and microglia/macrophage proliferation in the ischemic mouse brain. Glia *39*, 85–97. https://doi.org/10.1002/glia.10081.

43. Saijo, K., and Glass, C.K. (2011). Microglial cell origin and phenotypes in health and disease. Nat. Rev. Immunol. *11*, 775–787. https://doi.org/10.1038/nri3086.

44. Fernández-Arjona, M.D.M., Grondona, J.M., Fernández-Llebrez, P., and López-Ávalos, M.D. (2019). Microglial activation by microbial neuraminidase through TLR2 and TLR4 receptors. J. Neuroinflammation *16*, 245–314. https://doi.org/10.1186/s12974-019-1643-9.

45. Morrison, H., Young, K., Qureshi, M., Rowe, R.K., and Lifshitz, J. (2017). Quantitative microglia analyses reveal diverse morphologic responses in the rat cortex after diffuse brain injury. Sci. Rep. *7*, 13211. https://doi.org/10.1038/s41598-017-13581-z.

46. Fan, L., Young, P.R., Barone, F.C., Feuerstein, G.Z., Smith, D.H., and McIntosh, T.K. (1996). Experimental brain injury induces differential expression of tumor necrosis factor-α mRNA in the CNS. Brain Res. Mol. Brain Res. *36*, 287–291. https://doi.org/10.1016/0169-328X(95)00274-V.

47. Frugier, T., Morganti-Kossmann, M.C., O'Reilly, D., and McLean, C.A. (2010). In situ detection of inflammatory mediators in post mortem human brain tissue after traumatic injury. J. Neurotrauma *27*, 497–507. https://doi.org/10.1089/neu.2009.1120.

48. Mecha, M., Yanguas-Casás, N., Feliú, A., Mestre, L., Carrillo-Salinas, F.J., Riecken, K., Gomez-Nicola, D., and Guaza, C. (2020). Involvement of Wnt7a in the role of M2c microglia in neural stem cell oligodendrogenesis. J. Neuroinflammation *17*, 88. https://doi.org/10.1186/s12974-020-01734-3.

49. Halleskog, C., Dijksterhuis, J.P., Kilander, M.B.C., Becerril-Ortega, J., Villaescusa, J.C., Lindgren, E., Arenas, E., and Schulte, G. (2012). Heterotrimeric G protein-dependent WNT-5A signaling to ERK1/2 mediates distinct aspects of microglia proinflammatory transformation. J. Neuroinflammation *9*, 111. https://doi.org/10.1186/1742-2094-9-111.

50. Frakes, A.E., Ferraiuolo, L., Haidet-Phillips, A.M., Schmelzer, L., Braun, L., Miranda, C.J., Ladner, K.J., Bevan, A.K., Foust, K.D., Godbout, J.P., et al. (2014). Microglia induce motor neuron death via the classical NF-κB pathway in amyotrophic lateral sclerosis. Neuron *81*, 1009–1023. https://doi.org/10.1016/j.neuron.2014.01.013.

51. Lai, W., Ouyang, L., Liu, N., Liu, S., Shi, Y., Chen, L., Wang, X., Xiao, D., Liu, S., and Tao, Y. (2020). Identification of CpG Methylation and Non-CpG Methylation Is Associate with Lymphocyte Specific Helicase. https://doi.org/10.21203/rs.2.19979/v1.

52. Welser-Alves, J.V., and Milner, R. (2013). Microglia are the major source of TNF-α and TGF-β1 in postnatal glial cultures; Regulation by cytokines, lipopolysaccharide, and vitronectin. Neurochem. Int. *63*, 47–53. https://doi.org/10.1016/j.neuint.2013.04.007.

53. Del Zoppo, G.J., Milner, R., Mabuchi, T., Hung, S., Wang, X., Berg, G.I., and Koziol, J.A. (2007). Microglial activation and matrix protease generation during focal cerebral ischemia. Stroke *38*, 646–651. https://doi.org/10.1161/01.STR.0000254477.34231.cb.

54. Frik, J., Merl-Pham, J., Plesnila, N., Mattugini, N., Kjell, J., Kraska, J., Gómez, R.M., Hauck, S.M., Sirko, S., and Götz, M. (2018). Cross-talk between monocyte invasion and astrocyte proliferation regulates scarring in brain injury. EMBO Rep. *19*, e45294. https://doi.org/10.15252/embr.201745294.

55. Buffo, A., Rite, I., Tripathi, P., Lepier, A., Colak, D., Horn, A.-P., Mori, T., and Götz, M. (2008). Origin and progeny of reactive gliosis: a source of multipotent cells in the injured brain. Proc. Natl. Acad. Sci. USA *105*, 3581–3586. https://doi.org/10.1073/pnas.0709002105.

56. Vidoni, E.D., Acerra, N.E., Dao, E., Meehan, S.K., and Boyd, L.A. (2010). Role of the primary somatosensory cortex in motor learning: an rTMS study. Neurobiol. Learn. Mem. *93*, 532–539. https://doi.org/10.1016/j.nlm.2010.01.011.

57. Pavlides, C., Miyashita, E., and Asanuma, H. (1993). Projection from the sensory to the motor cortex is important in learning motor skills in the monkey. J. Neurophysiol. *70*, 733–741. https://doi.org/10.1152/jn.1993.70.2.733.

58. Mathis, M.W., Mathis, A., and Uchida, N. (2017). Somatosensory cortex plays an essential role in forelimb motor adaptation in mice. Neuron *93*, 1493–1503.e6. https://doi.org/10.1016/j.neuron.2017.02.049.

59. Nakamura, T., Sakai, K., Nakamura, T., and Matsumoto, K. (2011). Hepatocyte growth factor twenty years on: much more than a growth factor. J. Gastroenterol. Hepatol. *26*, 188–202. https://doi.org/10.1111/j.1440-1746.2010.06549.x.

60. Desole, C., Gallo, S., Vitacolonna, A., Montarolo, F., Bertolotto, A., Vivien, D., Comoglio, P., and Crepaldi, T. (2021). HGF and MET: from brain development to neurological disorders. Front. Cell Dev. Biol. *9*, 683609. https://doi.org/10.3389/fcell.2021.683609.

61. Zhao, L.-J., Wang, Z.-T., Ma, Y.-H., Zhang, W., Dong, Q., Yu, J.-T., and Tan, L.; Alzheimer's Disease Neuroimaging Initiative (2021). Associations of the cerebrospinal fluid hepatocyte growth factor with Alzheimer's disease pathology and cognitive function. BMC Neurol. *21*, 387. https://doi.org/10.1186/s12883-021-02356-9.

62. Chiaretti, A., Genovese, O., Aloe, L., Antonelli, A., Piastra, M., Polidori, G., and Di Rocco, C. (2005). Interleukin 1β and interleukin 6 relationship with paediatric head trauma severity and outcome. Childs Nerv. Syst. *21*, 185–193. https://doi.org/10.1007/s00381-004-1032-1.

63. Yan, E.B., Satgunaseelan, L., Paul, E., Bye, N., Nguyen, P., Agyapomaa, D., Kossmann, T., Rosenfeld, J.V., and Morganti-Kossmann, M.C. (2014). Post-traumatic hypoxia is associated with prolonged cerebral cytokine production, higher serum biomarker levels, and poor outcome in patients with severe traumatic brain injury. J. Neurotrauma *31*, 618–629. https://doi.org/10.1089/neu.2013.3087.

64. Ding, K., Wang, H., Xu, J., Lu, X., Zhang, L., and Zhu, L. (2014). Melatonin reduced microglial activation and alleviated neuroinflammation induced neuron degeneration in experimental traumatic brain injury: possible involvement of mTOR pathway. Neurochem. Int. *76*, 23–31. https://doi.org/10.1016/j.neuint.2014.06.015.

65. Kyyriäinen, J., Ekolle Ndode-Ekane, X., and Pitkänen, A. (2017). Dynamics of PDGFRβ expression in different cell types after brain injury. Glia *65*, 322–341. https://doi.org/10.1002/glia.23094.

66. Anandasabapathy, N., Victora, G.D., Meredith, M., Feder, R., Dong, B., Kluger, C., Yao, K., Dustin, M.L., Nussenzweig, M.C., Steinman, R.M., and Liu, K. (2011). Flt3L controls the development of radiosensitive dendritic cells in the meninges and choroid plexus of the steady-state mouse brain. J. Exp. Med. *208*, 1695–1705. https://doi.org/10.1084/jem.20102657.

67. Abella, J.V., Peschard, P., Naujokas, M.A., Lin, T., Saucier, C., Urbé, S., and Park, M. (2005). Met/Hepatocyte growth factor receptor ubiquitination suppresses transformation and is required for Hrs phosphorylation. Mol. Cell Biol. *25*, 9632–9645. https://doi.org/10.1128/mcb.25.21.9632-9645.2005.

68. Row, P.E., Clague, M.J., and Urbé, S. (2005). Growth factors induce differential phosphorylation profiles of the Hrs-STAM complex: a common node in signalling networks with signal-specific properties. Biochem. J. *389*, 629–636. https://doi.org/10.1042/BJ20050067.

69. Ito, M., Shichita, T., Okada, M., Komine, R., Noguchi, Y., Yoshimura, A., and Morita, R. (2015). Bruton's tyrosine kinase is essential for NLRP3 inflammasome activation and contributes to ischaemic brain injury. Nat. Commun. *6*, 7360. https://doi.org/10.1038/ncomms8360.

70. Pellerin, K., Rubino, S.J., Burns, J.C., Smith, B.A., McCarl, C.-A., Zhu, J., Jandreski, L., Cullen, P., Carlile, T.M., Li, A., et al. (2021). MOG autoantibodies trigger a tightly-controlled FcR and BTK-driven microglia proliferative response. Brain *144*, 2361–2374. https://doi.org/10.1093/brain/awab231.

71. Cohen, M.E., Fainstein, N., Lavon, I., and Ben-Hur, T. (2014). Signaling through three chemokine receptors triggers the migration of transplanted neural precursor cells in a model of multiple sclerosis. Stem Cell Res. *13*, 227–239. https://doi.org/10.1016/j.scr.2014.06.001.

72. Suzuki, Y., Funakoshi, H., Machide, M., Matsumoto, K., and Nakamura, T. (2008). Regulation of cell migration and cytokine production by HGF-like protein (HLP)/macrophage stimulating protein (MSP) in primary microglia. Biomed. Res. *29*, 77–84. https://doi.org/10.2220/biomedres.29.77.

73. Yamagata, T., Muroya, K., Mukasa, T., Igarashi, H., Momoi, M., Tsukahara, T., Arahata, K., Kumagai, H., and Momoi, T. (1995). Hepatocyte growth factor specifically expressed in microglia activated Ras in the neurons, similar to the action of neurotrophic factors. Biochem. Biophys. Res. Commun. *210*, 231–237. https://doi.org/10.1006/bbrc.1995.1651.

74. Nishikoba, N., Kumagai, K., Kanmura, S., Nakamura, Y., Ono, M., Eguchi, H., Kamibayashiyama, T., Oda, K., Mawatari, S., Tanoue, S., et al. (2020). HGF-MET signaling shifts M1 macrophages toward an M2-like phenotype through PI3K-mediated induction of arginase-1 expression. Front. Immunol. *11*, 2135. https://doi.org/10.3389/fimmu.2020.02135.

75. Zhao, L., Wu, Y., Xie, X.D., Chu, Y.F., Li, J.Q., and Zheng, L. (2015). C-Met identifies a population of matrix metalloproteinase 9-producing monocytes in peritumoural stroma of hepatocellular carcinoma. J. Pathol. *237*, 319–329. https://doi.org/10.1002/path.4578.

76. Benkhoucha, M., Senoner, I., and Lalive, P.H. (2020). C-Met is expressed by highly autoreactive encephalitogenic CD8+ cells. J. Neuroinflammation *17*, 68. https://doi.org/10.1186/s12974-019-1676-0.

77. Gordin, M., Tesio, M., Cohen, S., Gore, Y., Lantner, F., Leng, L., Bucala, R., and Shachar, I. (2010). c-Met and its ligand hepatocyte growth factor/scatter factor regulate mature B cell survival in a pathway induced by CD74. J. Immunol. *185*, 2020–2031. https://doi.org/10.4049/jimmunol.0902566.

78. Organ, S.L., and Tsao, M.S. (2011). An overview of the c-MET signaling pathway Therapeutic Advances in Medical Oncology. Ther. Adv. Med. Oncol. *3*, S7–S19. https://doi.org/10.1177/1758834011422556.

79. Beilmann, M., Vande Woude, G.F., Dienes, H.P., and Schirmacher, P. (2000). Hepatocyte growth factor-stimulated invasiveness of monocytes. Blood *95*, 3964–3969. https://doi.org/10.1182/blood.v95.12.3964.012k20_3964_3969.

80. Choi, W., Lee, J., Lee, J., Lee, S.H., and Kim, S. (2019). Hepatocyte growth factor regulates macrophage transition to the M2 phenotype and promotes murine skeletal muscle regeneration. Front. Physiol. *10*, 914. https://doi.org/10.3389/fphys.2019.00914.

81. Coudriet, G.M., He, J., Trucco, M., Mars, W.M., and Piganelli, J.D. (2010). Hepatocyte growth factor modulates interleukin-6 production in bone marrow derived macrophages: implications for inflammatory mediated diseases. PLoS One *5*, e15384. https://doi.org/10.1371/journal.pone.0015384.

82. Hosonuma, M., Sakai, N., Furuya, H., Kurotaki, Y., Sato, Y., Handa, K., Dodo, Y., Ishikawa, K., Tsubokura, Y., Negishi-Koga, T., et al. (2021). Inhibition of hepatocyte growth factor/c-Met signalling abrogates joint destruction by suppressing monocyte migration in rheumatoid arthritis. Rheumatology *60*, 408–419. https://doi.org/10.1093/rheumatology/keaa310.

83. Fujikawa, R., and Jinno, S. (2022). Identification of hyper-ramified microglia in the CA1 region of the mouse hippocampus potentially associated with stress resilience. Eur. J. Neurosci. *56*, 5137–5153. https://doi.org/10.1111/ejn.15812.

84. Costello, A., Linning-Duffy, K., Vandenbrook, C., Lonstein, J.S., and Yan, L. (2022). Daytime light deficiency leads to sex- and brain region-specific neuroinflammatory responses in a diurnal rodent. Cell. Mol. Neurobiol. https://doi.org/10.1007/s10571-022-01256-x.

85. Hinwood, M., Tynan, R.J., Charnley, J.L., Beynon, S.B., Day, T.A., and Walker, F.R. (2013). Chronic stress induced remodeling of the prefrontal cortex: structural Re-organization of microglia and the inhibitory effect of minocycline. Cerebr. Cortex *23*, 1784–1797. https://doi.org/10.1093/cercor/bhs151.

86. Smith, K.L., Kassem, M.S., Clarke, D.J., Kuligowski, M.P., Bedoya-Pérez, M.A., Todd, S.M., Lagopoulos, J., Bennett, M.R., and Arnold, J.C. (2019). Microglial cell hyper-ramification and neuronal dendritic spine loss in the hippocampus and medial prefrontal cortex in a mouse model of PTSD. Brain Behav. Immun. *80*, 889–899. https://doi.org/10.1016/j.bbi.2019.05.042.

87. Dissing-Olesen, L., LeDue, J.M., Rungta, R.L., Hefendehl, J.K., Choi, H.B., and MacVicar, B.A. (2014). Activation of neuronal NMDA receptors triggers transient ATP-mediated microglial process outgrowth. J. Neurosci. *34*, 10511–10527. https://doi.org/10.1523/JNEUROSCI.0405-14.2014.

88. Flierl, M.A., Stahel, P.F., Beauchamp, K.M., Morgan, S.J., Smith, W.R., and Shohami, E. (2009). Mouse closed head injury model induced by a

weight-drop device. Nat. Protoc. *4*, 1328–1337. https://doi.org/10.1038/nprot.2009.148.

89. Rogg, J., Spader, H., Wilcox, B.J., Ellermeier, A., Correira, S., Chodobski, A., Szmydynger-Chodobska, J., Raukar, N., Machan, J.T., Crisco, J.J., and LaFrance, W.C.; Brown University Traumatic Brain Injury Research Consortium (2014). The Brown university traumatic brain injury research consortium and the norman prince neurosciences institute. R. I. Med. J. *97*, 22–26.

90. Gyoneva, S., Kim, D., Katsumoto, A., Kokiko-Cochran, O.N., Lamb, B.T., and Ransohoff, R.M. (2015). Ccr2 deletion dissociates cavity size and tau pathology after mild traumatic brain injury. J. Neuroinflammation *12*, 228. https://doi.org/10.1186/s12974-015-0443-0.

91. Rehman, R., Tar, L., Olamide, A.J., Li, Z., Kassubek, J., Böckers, T., Weishaupt, J., Ludolph, A., Wiesner, D., and Roselli, F. (2021). Acute TBK1/IKK-ε inhibition enhances the generation of disease-associated microglia-like phenotype upon cortical stab-wound injury. Front. Aging Neurosci. *13*, 684171. https://doi.org/10.3389/fnagi.2021.684171.

92. Rehman, R. (2020). Rida-Rehman/PROTEAS: PROTein expression AnalysiS. GitHub. https://github.com/Rida-Rehman/PROTEAS.

STAR★METHODS

KEY RESOURCES TABLE

REAGENT or RESOURCE	SOURCE	IDENTIFIER
Antibodies		
Mouse anti-NeuN	Abcam	Cat# PA5-78499, RRID: AB_2736206
Rabbit anti-GFAP	Abcam	Cat# Ab4674, RRID: AB_305808
Chicken anti-GFAP	Abcam	Cat# Ab4674, RRID: AB_304558
Rabbit anti-pMet/HGFR (Tyr1234)	Cell signaling	Cat# 3077S, RRID: AB_628123
Rabbit anti-pMet/HGFR (Tyr1234)	R&D systems	Cat# AF2480, RRID: AB_416603
Rabbit anti-pBTK (Tyr222)	Novus biologicals	Cat# NBP1-78295, RRID: AB_11032627
Rabbit anti-pVEGFR1 (Tyr1333)	Biorbyt	Cat# orb644609, RRID: AB_2924912
Rabbit anti-HELLS	Antibodies.com	Cat# A34212, RRID: AB_2924912
Rat anti-Vitronectin	R&D systems	Cat# MAB38751, RRID: AB_2216439
Mouse anti-Integrin beta 3	Novus biologicals	Cat# NB600-1342, RRID: AB_10003443
Guinea pig anti-Iba1	Synaptic systems	Cat# 234004, RRID: AB_2493179
Lycopersicon Esculentum (Tomato) Lectin (LEL, TL), DyLight® 594	Vector labs	Cat# DL-1177-1, RRID: AB_2336416
Rabbit anti-Cd11c	Synaptic Systems	Cat# 375 003, RRID: AB_2630323
Mouse anti-Cd68	Abcam	Cat# ab31630, RRID: AB_1141557
Rabbit anti-Ki67	Thermo Scientific	Cat# RM-9106-S0, RRID: AB_2341197
Chicken anti-Tmem119	Synaptic Systems	Cat# 400 006, RRID: AB_2744643
Rabbit anti-NF-kappa-ß-P65	CST	Cat# 8242T, RRID: AB_10859369
Chemicals, peptides, and recombinant proteins		
Alexa Fluor 488 Tyramide SuperBoost Kit	Invitrogen	B40922
JNJ-38877605	Selleckchem	HY50683
Spebrutinib (CC-292)	Selleckchem	S7173
Valatanib (PTK-787)	MedChemExpress	HY-12018
Critical commercial assays		
Proteome Profiler Mouse Phospho-RTK Array Kit	R&D systems	ARY014
Full Moon Tyrosine phosphorylation array	Full Moon Biosystems	PCS300
Antibody array assay kit	Full Moon Biosystems	KAS02
SIMOA IL-6 Advantage Kit	Quanterix	101622
SIMOA IL-1b Advantage Kit	Quanterix	101605
Deposited data		
Proteomics data	PRIDE database	PRIDE: PXD037500
Software and algorithm		
Image J	NIH	RRID: SCR_003070
Prism 7.0	GraphPad Software	RRID: SCR_002798
R studio	R	NA
GenePix Pro Software v7	Molecular Devices LLC	RRID: SCR_010969
Other		
LEICA Confocal microscope	DMi8 S Platform	NA
GenePix 4000B Microarray Scanner	Molecular Devices LLC	GENEPIX 4000B-U

RESOURCE AVAILABILITY

Lead contact

Further information and requests for resources and reagents should be directed to and will be fulfilled by the lead contact, Francesco Roselli (francesco.roselli@uni-ulm.de). Any additional information required to reanalyze the data reported in this paper is available from the lead contact upon request.

Materials availability

All reagents generated in this study are available from the lead contact.

Data and code availability

- All data reported in this paper will be shared by the lead contact upon request.
- The code used in the study has been made public on the GitHub repository; github.com/Rida-Rehman/PROTEAS.
- Any additional information required to reanalyze the data reported in this paper is available from the lead contact upon request.
- The proteomics data are available on PRIDE database via ProteomeXchange with identifier PRIDE: PXD037500 (http://www.ebi.ac.uk/pride).

EXPERIMENTAL MODEL AND SUBJECT DETAILS

Mouse strains

All experimental procedures were performed in compliance with animal protocols approved by the local veterinary and animal experimentation committee at University Ulm, Germany under the license number 1370 (blunt TBI) or 1379 (stab wound injury) or by the institutional ethical committee of KU Leuven with license number P021-2017. B6SJL male mice aged between p60–p90 days were used throughout the study. Mice were kept in animal house with 12/12h sleep wake cycle. Food and water were provided and cages cleaned as needed or after 1 week.

Human CSF samples

CSF samples from TBI patients were obtained at the Alfred Hospital, Melbourne and was approved by the Alfred ethical committee and by the ethical committee of Ulm University (license 194/05). Informed consent for the sampling of CSF was obtained from the next of the kin; data regarding the original cohort have been previously published.[63] Inclusion criteria were: severe TBI with a post-resuscitation GCS $\leq$8 (unless initial GCS>9 was followed by deterioration requiring intubation) and, upon CT imaging, the need for an extra ventricular drain (EVD) for ICP monitoring and therapeutic drainage of CSF. Exclusion criteria comprised pregnancy, neurodegenerative diseases, HIV and other chronic infection/inflammatory diseases, or history of TBI. CSF was collected over 24 h and kept at 4°C. Samples were obtained on admission (day 0), in the first 24h (day 1) and three days after injury (day 3). CSF samples were centrifuged at 2000g for 15 min at 4°C and stored at −80°C until analysis. Out of the 42 TBI patients constituting the original cohort,[63] we selected samples from 30 patients, depending on the availability of three aliquots for day 0, day 1 and day 3 after injury (Clinico-demographic details available in Table S5).

Traumatic brain injury (TBI) model

For all surgical procedures, mice were anesthetized with sevoflurane/isoflurane (2–4% in 96% O2) and were subcutaneously injected with buprenorphine (0.1mg/kg) as a pre- or postoperative analgesic. TBI was induced in mice by a modified closed, blunt weight drop model.[88] The scalp was shaved and eye ointment was applied post-operatively to protect the cornea. Scalp skin was then incised on the midline to expose the skull and the animals were positioned in the weight-drop apparatus in which the head was secured to a holding frame. Using the 3-axis mobile platform in the apparatus, the impactor was positioned to the coordinates of the injection site (from bregma x = +3.0mm, y = − 2.0mm, z = 0.0mm). TBI was delivered by dropping a weight of 120/125g from a height of 45 cm (or 40 cm for low impact). A mechanical stop prevented a skull displacement (by the impactor) larger than 2.5 mm, in order to limit brain damage. The overall time of mice exposure to sevoflurane/isoflurane did not exceed 10 mins. After restoration of normal breathing, mice were removed from the stereotactic frame. The skin was sutured with proline 6.0 surgical thread and the mice were left on the heating pad until regained consciousness. Severity of the trauma was assessed by the Neurological Severity Score at 2h[14]. All mice used in the present study had NSS ranging between 0 and 1. Animals were then transferred to recovery cage ad libitum access to food and water. Animals were sacrificed at 3h (corresponding approximately to the time-to-triage in human mild TBI patients[89]) and at 1-, 3- and 7-days post injury (approximately corresponding to different stages of injury evolution[90]). Effort was made to minimize the suffering of animals and reduce the number of animals used.

Stab wound injury (SWI) model

The stab wound injury (SWI) was used as a second injury model in the study.[54,91] Briefly, mice aged p60-90 were anesthetized with an intraperitoneal injection of midazolam, medetomidine, and fentanyl (5 mg/kg; 0.5 mg/kg; 0.05 mg/kg). A unilateral craniotomy was performed. The blade was inserted into the primary motor cortex up to a depth of 0.8 mm (z = −0.8) and moved 1 mm in the dorsal direction. Three parallel stab-injuries were performed with a gap of 0.2 mm. This gap was chosen so that the three injuries would actually form a single lesion area. The health status of the animals was monitored after the procedure and until the end of the experiment. The skin was sutured with proline 6.0 surgical thread and the mice were left on the heating pad until regained consciousness. Animals were sacrificed at 3h. Effort was made to minimize the suffering of animals and reduce the number of animals used.

METHOD DETAILS

Antibodies

Primary antibodies used were: Mouse anti-NeuN (1:100, Abcam), Rabbit anti-GFAP (1:500, Abcam), Rabbit anti-pMet/HGFR (1:200, Cell Signaling/R&D systems), Rabbit anti-pBTK (1:200, Novus Biologicals), Rabbit anti-pVEGFR1 (1:200, Biorbyt), Rabbit anti-HELLS (1:100, Antibodies.com), Rat anti-Vitronectin (1:100, R&D systems), Mouse anti-Integrin beta 3 (1:50, Novus biologicals), Guinea pig anti-Iba1 (1:500, Synaptic systems), Chicken anti-GFAP (1:500, Abcam), Lycopersicon Esculentum (Tomato) Lectin (LEL, TL), DyLight® 594 (1:100, Vector labs), Rabbit anti-Cd11c (1:500, Synaptic Systems), Mouse anti-Cd68 (1:200, Abcam), Rabbit anti-Ki67 (1:500, Thermo Scientific), Chicken anti-Tmem119 (1:500, Synaptic Systems), Rabbit anti-NF-kappa-ß-P65 (1:100, CST). Secondary antibodies were used from Invitrogen or Life Technologies, raised in either goat or donkey against primary antibody's host species, highly crossed absorbed and conjugated to fluorophores of Alexa Fluor 488, Alexa Fluor 568, Alexa Fluor 647 and used at a 1:500 dilution. Alexa Fluor 405 conjugated DAPI was used at 1:1000 dilution. For signal amplification, streptavidin conjugated to Alexa Fluor 488 (1:1000, Life Technologies) was used to amplify against the biotin tag.

Perfusions and tissue processing

Animals were given an overdose of anesthesia and transcardially perfused with 25 mL ice cold PBS 0.5M EDTA followed by 50mL 4% paraformaldehyde (PFA). After perfusion, brains were dissected and post fixed in 4% PFA overnight at 4°C. Tissues were cryo protected by sinking in 30% sucrose in PBS. Samples were frozen in the Optimal Cutting Temperature (OCT) compound (Tissue Tek, Sakura) using dry ice. 40 μm thick free-floating sections, spanning the injection/TBI site (identified using coordinates, appearance of third and lateral ventricles, corpus callosum using Allen brain Atlas as reference) were cut in a cryostat, collected in PBS and processed for immunostaining.

Protein extraction

Mice were sacrificed at respective timepoints (or sham surgery in case of control) by placing them in heavy sevoflurane filled containers. Once the animals stopped breathing, they were removed from the container and the brain was quickly dissected in cold PBS. Tissue samples (∅ 0.25 cm) were punched from the lesioned and contralateral uninjured somatosensory cortex and immediately frozen at −80°C.

For the arrays, samples were then thawed in RIPA buffer prepared in house (150mM NaCl, 10mM Tris, 0.1% Sodium Dodecyl Sulfate (SDS), 1% Triton 100X and 5mM EDTA) containing Phosphatase (1 tablet per 3.3mL lysis buffer) and Protease (1 tablet per 16.67mL lysis buffer) inhibitor (Roche complete tablets, Sigma-Aldrich, Taufkirchen, Germany) cocktail and homogenized with approximately 20 strokes of Dounce apparatus. Tissue homogenates were then cleared by centrifugation twice (10.000g, 10min and 10.000g, 5 mins) and assayed for protein concentration using the BSA kit from ThermoFisher.

Phospho RTK array processing

Proteome Profiler Mouse Phospho-RTK Array Kit (R&D Systems, Minneapolis) was used to determine the Phospho RTK activation pattern. The nitrocellulose membrane arrays provided in the kit were based on sandwich immunoassay and processed according to manufacturer's instructions. Briefly, membranes spotted with the anti-RTK antibody were blocked in Array buffer 1 for 1h at RT. 130 ug of extracted protein was diluted in 1.5mL Array buffer 1 overnight at 4°C.

The membranes were then washed 3 × 10 min in Wash Buffer and incubated for 2 h at RT with Anti-Phospho-Tyrosine-HRP Detection Antibody, diluted to 1:5000 in 1X Array Buffer 2. After final washing steps, HRP detection was performed by adding 1 mL Clarity Max^{TM} Western ECL Blotting Substrates from Bio-Rad. Arrays were imaged using BioRad X-ray imager and quantified using ImageJ. ROI was drawn on each antibody spot with a constant diameter and mean gray value was recorded. Further analysis was performed using R software.

Tyrosine kinase array processing

Tyrosine phosphorylation proarray (Full moon Biosystems, Sunnyvale, CA) were used to determine the phosphorylation of 228 phosphorylation targets. The arrays were processed according to the manufacturer's instructions. Briefly, the sample was biotinylated with Biotin/DMF solution for 2 h at RT with episodic vortex. The solution was mixed with reaction stop reagent and incubated for 30 mins at RT. The glass arrays were incubated in a blocking solution for 45 minutes and washed 10 times with distilled water until the slide was smooth without any residue. After adding a biotinylated sample to the coupling solution, arrays were incubated for 2h at RT and washed with 1X wash buffer three times for 10 mins. The arrays were washed again with distilled water (G biosciences) and incubated with a detection buffer with Cy5-streptavidin (ThermoFisher) at 1:1000 for 20 minutes at RT protected from light. The washing steps were repeated as described above. After removing excess water from the slides, the arrays were dried using 10 psi compressed air at a 30-degree angle with 2-inch distance between the nozzle and the glass slide. The arrays were images using GenePix 4000B array scanner (Molecular Devices, LLC) and the image analysis was performed using GenePix Pro Software v7 (Molecular Devices, LLC). The settings for the analysis were kept constant in all cases. The GAL file was loaded in the software and the ROI was adjusted on the protein spots. Each intensity was recorded and GPR files were saved.

Proteomics (mass spectrometry) measurement and analysis

Samples collected at 3h, 3d and 7d were processed and analyzed together. Liquid Chromatography with Tandem Mass Spectrometry (LC-MS/MS) measurement was performed in data-independent acquisition (DIA) mode on a Q-Exactive HF mass spectrometer (Thermo Scientific) coupled online to a nano-RSLC (Ultimate 3000 RSLC; Dionex). Tryptic peptides were automatically loaded on a C18 trap column (300 μm inner diameter (ID) × 5 mm, Acclaim PepMap100 C18, 5 μm, 100 Å, LC Packings) at 30μL/min flow rate. For chromatography, a C18 reversed phase analytical column (nanoEase MZ HSS T3 Column, 100Å, 1.8 μm, 75 μm × 250 mm, Waters) at 250nL/min flow rate in a 120 minutes non-linear acetonitrile gradient from 3 to 40% in 0.1% formic acid was used. The DIA method consisted of a survey scan from 300 to 1,650 mass-to-charge ratio at 120,000 resolution and an automatic gain control (AGC) target of 3e6 or 120 ms maximum injection time. Fragmentation was performed via higher energy collisional dissociation with a target value of 3e6 ions determined with predictive AGC. Precursor peptides were isolated with 37 variable windows spanning from 300 to 1,650 mass-to-charge ratio at 30,000 resolutions with an AGC target of 3e6 and automatic injection time. The normalized collision energy was 28, and the spectra were recorded in profile mode.

For label-free quantification, the LC−MS/MS data set was analyzed using Spectronaut (Version 13, Biognosys, Schlieren, Switzerland) with default settings for the spectral library search. Automatic calibration mode was chosen with precision iRT enabled for applying the nonlinear iRT calibration strategy. Peptide identification was filtered to satisfy FDR = 0.01. Only proteotypic peptides were considered for protein quantification applying summed precursor quantities based on MS2 area quantity. Match between runs was enabled with the data filtering function set to q-value percentile mode applying the 10% setting. For this study, we have only included 3hpi results while 3dpi and 7dpi results will be published in subsequent study. Proteomic data are available on PRIDE database via ProteomeXchange with identifier PXD037500.

Pharmacological agents and treatment procedures

The BTK inhibitor CC-292 (Selleckchem chemicals, Munich, Germany), Met inhibitor JNJ38877605 (Medchem) and VEGFR1 inhibitor Vatalanib (PTK787) 2HCl (Selleckchem chemicals, Munich, Germany) are commercially available. Drugs were dissolved in a minimal volume of DMSO; CC-292 10mg in 50ul, JNJ38877605, 10mg in 150 ul, PTK787, 10mg in 100ul. The selected doses were dissolved in 200 ul of vehicle (90% saline, 5% PEG 400 and 5% Tween 80) maintaining the concentration of DMSO less than 5% in the final dose. The inhibitors were orally administered at doses 2 h before the trauma in order to obtain an approximated peak systemic concentration at the moment of trauma, based on available pharmacokinetic data. For longer inhibitor treatment in behavior experiments, drug or saline was administered 2h before trauma for a period of 7 consecutive days. For each successive day, dose was administered immediately after the behavior session.

Immunostaining

Before blocking, antigen retrieval was performed by incubating the sections in Sodium Citrate Buffer (10mM Sodium Citrate, 0.05% Tween 20, pH 6.0) in a hot water bath (75°C) for 45 minutes. For phosphorylated proteins, sections were then subjected to hydrogen peroxide (0.3% H_2O_2) treatment for 20–30 minutes to quench the endogenous peroxidase activity. Sections were then blocked in a blocking buffer (3% BSA, 0.3% Triton in PBS) for 2h at 24 °C on a rotary shaker. Following blocking an appropriate mix of primary antibodies were diluted in the blocking buffer and incubated for 48 h at 4 °C. For staining against phosphorylated proteins, sections were then incubated in poly-HRP-conjugated secondary antibody or HRP-conjugated streptavidin from Alexa Fluor 488 Tyramide SuperBoost Kit (Invitrogen) for 60 minutes and then incubated in Tyramide working solution according to manufacturer's protocol. After incubating in Reaction stop reagent for 8 mins, sections were washed in PBS for 3 × 30 min and incubated in the appropriate mix of other secondary antibodies, together with, whenever appropriate, the DNA dye TOPRO-3 (1:1000, Invitrogen), diluted in a blocking buffer for 2h at 24 °C. After further washing the sections for 3 × 30 min in PBS, the sections were mounted on coverslips and onto the slides using FluoroGold Plus (Invitrogen).

Western blotting

Protein lysates were prepared using Radioimmunoprecipitation assay (RIPA) buffer (150 mM NaCl, 10 mM Tris pH 7,6, 0,1% SDS, 1% Triton X-100, 5 mM EDTA). Protease (Roche) and phosphatase inhibitors (Sigma Aldrich) were added to the buffer. Protein concentrations in the samples were determined using the BCA assay kit (Thermo Fisher Scientific). The Protein samples (60 μg) were then run on an 8–10% gel for 2 h at 60V and transferred to a nitrocellulose membrane. The membranes were blocked for 1 h at room temperature with 5% skim milk powder or 5% BSA dissolved in Tris-Buffered Saline-Tween (TBS-T), followed by an overnight incubation of primary antibodies at 4°C. The blots were then incubated in a secondary goat conjugated IgG-HRP antibody (rabbit or mouse; depending on the primary host) for 1h at RT. The blots were visualized using ECL-immunodetection. Samples were corrected for background and quantified using BIORAD Image Lab Software® 5.0, following manufacturer's procedures. All values were normalized first to the housekeeping genes (β-actin) and then to their respective total protein.

Microscopy

Confocal images were acquired using a LEICA DMi8 S inverted microscope, fitted with a 10× air or 20× oil objective. Tile-scans of 5 × 3 was acquired to cover the full span of the injury site and the full cortical thickness. The images were acquired in a 12-bit format. Imaging parameters (laser power, photomultiplier voltage, digital gain, and offset) were established with the goal of preventing

saturation in target structures while obtaining a lowest signal intensity of at least 150 (in arbitrary units). Image capture and processing conditions were kept constant when imaging was used for quantification. Brightness and contrast of images are adjusted and pseudo-colored for presentation.

Behavioral performance and assessment

The overall neurological/motor impairment was evaluated using forelimb reaching task recorded using four high-speed cameras (200 frames/second) for subsequent analysis. Animals were trained for 10 days for 20 minutes to extract food pellets from a narrow slit using their forelimbs. Food was restricted 2 h after the training session until the next session or conclusion of the experiment. Exclusions were made based on a 10% reduction in body weight of animals. After the training period, pre-treatment recordings were made. Post trauma recordings were made after 1, 3, 5, 7, 10, 14, 17 and 21 days. The analysis was performed by manually counting four modular aspects of forelimb movement. The trial was considered only if the paw is extended outside the plexiglass slit; (i) success; retrieving the pellet inside the container, (ii) failure (reach); unable to reach food due to problem in to assess sensorimotor impairments due to TBI, (iii) failure (grasp); reaches the pellet but unable to grasp it properly and (iv) failure (retrieval); hold the pellet but unable to retrieve inside the container. Percentages for the recorded trials for all four conditions were recorded by averaging against respective total trials per animal per session and analysis were performed by comparing groups with pretreatment (for TBI group) or subsequent time points among different groups.

In situ hybridization

Single-molecule *in situ* mRNA hybridization was performed according to manufacturer instructions (ACDBio, RNAscope, Fluorescence in Situ mRNA Hybridization for histological sections, all reagents/buffers were provided by ACDbio) with some modifications. Briefly, slides were mounted on glass slides. Target retrieval was performed for 3 min and sections were washed with dH20 and ethanol. Thereafter, slides were pretreated with protease III for 20 min at 40 °C and probe hybridization (for Wnt5a, TNFa, HGF and C3) was performed for 4.5 h at 40 °C, followed by 2 × 2 min washing step with washing buffer (provided by ACDbio) and 30 min incubation of amplification-1 reagent at 40 °C. Slides were washed 2 × 2 min and incubated with amplification-2 reagent for 15 min at 40 °C followed by another 2 × 2 min washing step. The last amplification was performed by 30 min incubation with amplification-3 followed by a 2 × 2 min washing step. A final detection amplification was performed by incubating the amplification-4 reagent for 45 min at 40 °C and the final washing step was increased to 2 × 10 min. The co-immunostaining procedure was performed soon after as follows: slides were blocked for 1 h in 10% BSA, 0,3% Triton in PBS and incubated overnight with primary antibody (Guinea pig anti-Iba1, 1:500 [abcam] and mouse anti-NeuN, 1:500 [abcam]). Slides were washed 3 × 30 min and incubated with secondary antibodies (Donkey anti-mouse 405, 1:500 [invitrogen] and Donkey anti-guinea pig 647 [Invitrogen]). After the last round of washing (3 × 30 min in PBS), the slides were mounted using Fluorogold prolong antifade mounting medium (Invitrogen)

ELISA and SIMOA assays

Single-molecule arrays were performed as per manufacturer instructions (Quanterix) for the quantification of IL-6 and IL-1β. CSF samples were diluted 1:20 for IL-6 measurements and diluted 1:5 for IL-1β measurements. The assay was then read on HD-1 Analyzer (Quanterix, USA). HGF levels in CSF were measured by sandwich ELISA for HGF (DuoSet Kit, R&D Systems, Minneapolis, MN, USA), as described by the manufacturer. The detection range was 125–8000 pg/mL for HGF. Undiluted CSF samples were used and the assay was read on a microplate reader set to 450 nm wavelength.

QUANTITATIVE AND STATISTICAL ANALYSIS

Array analysis

Chemiluminescence signal for each spot was logged after microarray image analysis. The raw intensity values for each receptor/protein were recorded automatedly via image recorder software or manually using ImageJ software. The raw data files were loaded in R software and the dataset for each array was preliminary subjected to quality control assessment (QCA); outlier identification, data distribution, intra-array and inter-array normalization. Normalized data for each array was subjected to principal component analysis (PCA) to display group-based clustering. Confidence ellipses (assuming multivariate normal distribution) with the first two principal components were plotted to validate further analysis. Modified linear modeling-based analysis was then applied to the data to identify RTK showing a significant increase or decrease in phosphorylation at the different timepoints. For protein array analyses, the code has been made publicly available on open-access GitHub repository PROTEAS.[92]

Image analysis

Region of interest was 2 × 10μm^2 and kept constant for all analyses. For the measurement of NeuN+ cells, Iba1+ cells and GFAP+ cells, 5 × 3 composite tiles cans of confocal stacks were acquired with the 10× objective to image the injury site and the surrounding penumbral and perilesional areas. Confocal stacks of 10–12 optical sections (at the same depth) were collapsed in maximum-intensity projections in ImageJ and a threshold was set for the resulting images, to establish a reproducible criterion. Regions of Interests

(ROIs) were positioned centered on the axis of the injury site. In these ROIs, the number of NeuN+ cells and/or GFAP+ cells were manually counted. At least 3–5 tissue sections were analyzed from each of 3–6 mice per experimental group.

For p-Met, pBTK, pVEGFR1, Vitronectin and HELLS fluorescence intensity analysis, confocal stacks composed of 19–21 optical sections (acquired at the same depth in the tissue section) were collapsed in maximum-intensity projections using the ImageJ software and a threshold was set for the resulting images, to establish a reproducible criterion. Microglia and neurons were identified based on their morphology, size and positive immunostaining for the microglial marker (Iba1) and neuronal marker (NeuN), respectively. A constant target region was considered for each experiment, spanning the cortical layer II–III and centered on the axis of the injury site. ROIs encompassing the cellular soma (excluding the nucleus for neurons) were manually drawn for each cell in the target region and the integrated average fluorescence intensity was logged. A minimum of 100 cells (layer II–III) from 3 distinct tissue sections from each of 3–5 mice were quantified. The median fluorescence intensity of phosphorylated receptors was computed. Microglia morphology was quantified using ImageJ skeleton and fractal analysis procedures as mentioned in (Morrison et al., 2018).

For Integrin beta 3 intensity analysis, confocal stacks composed of 19–21 optical sections (acquired at the same depth in the tissue section) were collapsed in maximum-intensity projections using the ImageJ software and a threshold was set for the resulting images, to establish a reproducible criterion. A target region was considered, spanning the cortical layer II–III and centered on the axis of the injury site. Vessels were stained using a vascular marker (Collagen IV) and area was recorded for a minimum 20 vessels of variable lengths in each section. After applying intensity threshold, positive area for Integrin beta 3 across these vessel lengths were recorded and normalized to compute the percentage of positive area.

Statistical analysis

Statistical analysis was performed with the GraphPad Prism software suite. Mann-Whitney U-Test was used for two group comparisons, One-way ANOVA with Bonferroni Correction was performed among three groups and Two-way ANOVA with Tukey correction was used for four group comparisons to examine statistical significance. Protein array analysis was performed using R software. Boxplots display the 25–75 percentile interval (box contours), and the full range (whiskers); for histograms, average ±standard deviation is used. Whenever opportune, we present individual measures datapoints (black, small size) and average per animal (green, large size). The statistical comparison is always performed using the number of animals as biological units; the individual datapoints are depicted to illustrate the distribution of the raw data. Statistical significance was set at $p < 0.05$.

ADDITIONAL RESOURCES

Code used for array analysis: https://github.com/Rida-Rehman/PROTEAS.